

**Anatectic melt inclusions in ultra-high temperature
 granulites**

Journal:	<i>Journal of Metamorphic Geology</i>
Manuscript ID	JMG-20-0024.R1
Manuscript Type:	Original Article
Date Submitted by the Author:	n/a
Complete List of Authors:	Gianola, Omar; University of Padua, Department of Geosciences Bartoli, Omar; Università di Padova, Dipartimento di Geoscienze Ferri, Fabio; Università degli studi di Padova Dipartimento di Geoscienze, Dipartimento di Geoscienze Galli, Andrea; Department of Earth Sciences, ETH Zurich, Sonneggstrasse 5 Ferrero, Silvio; Universität Potsdam, Institut für Erd- und Umweltwissenschaften Capizzi, Luca; Università degli Studi di Roma La Sapienza, Dipartimento di Scienze della Terra Liebske, Christian; ETH Zürich, Department of Earth Sciences Remusat, Laurent; Muséum National d'Histoire Naturelle, Sorbonne Université, Institut de Minéralogie, de Physique des Matériaux et de Cosmochimie Poli, Stefano; Università degli Studi di Milano, Department of Earth Sciences "Ardito Desio" Cesare, Bernardo; Università degli Studi di Padova, Dept. Geosciences
Keywords:	Fluid inclusions, Garnet, Granites, Gruf Complex, Nanogranitoids

1 **Title: Anatectic melt inclusions in ultra-high temperature granulites**

2 **Omar Gianola**¹, Omar Bartoli¹, Fabio Ferri¹, Andrea Galli², Silvio Ferrero³, Luca S.

3 Capizzi^{1,4}, Christian Liebske², Laurent Remusat⁵, Stefano Poli⁶, Bernardo Cesare¹

4 ¹ Dipartimento di Geoscienze, Università degli Studi di Padova, Via G. Gradenigo 6, 35131 Padova,

5 Italy

6 ² Institute of Geochemistry and Petrology, ETH Zürich, Switzerland

7 ³ Institut für Erd- und Umweltwissenschaften, Universität Potsdam, Potsdam, Germany

8 ⁴ Dipartimento di Scienze della Terra, Università degli Studi di Roma “La Sapienza”, Roma, Italy

9 ⁵ Institut de Minéralogie, de Physique des Matériaux, et de Cosmochimie (IMPMC), UMR CNRS

10 7590 – Sorbonne Université – Muséum National d'Histoire Naturelle, Paris, France

11 ⁶ Dipartimento di Scienze della Terra “Ardito Desio”, Università degli Studi di Milano, Milano, Italy

12

13

14

15

16

17

18

19

20

21

22 Abstract

23 Partial melting up to ultra-high temperature (UHT) conditions is one of the major processes
24 for the geochemical differentiation and reworking of the mid- to lower continental crust, with
25 relevant implications on its rheological behaviour. UHT granulites from the Gruf Complex
26 (European Central Alps) display garnet and sapphirine porphyroblasts containing a variety of
27 primary melt inclusions. Typically, melt inclusions in garnets occur as glassy and
28 polycrystalline inclusions (i.e. nanogranitoids), the latter often organized in mm-sized
29 clusters associated with primary fluid inclusions. Nanogranitoids are characterized by an
30 elliptical faceted shape, with variable sizes ranging from 2 to 115 μm , while glassy inclusions
31 show negative crystal shapes that usually never exceed 15 μm in diameter and present CO_2 -
32 rich shrinkage bubbles. The characteristic mineral assemblage observed in nanogranitoids
33 consists of quartz, biotite, muscovite, plagioclase, K-feldspar, kokchetavite and rarely
34 aluminosilicates. Glassy and re-homogenized melt inclusions are peraluminous and rhyolitic
35 in composition, with $\text{SiO}_2 = 69\text{-}80 \text{ wt}\%$ and $\text{Na}_2\text{O}+\text{K}_2\text{O} = 5\text{-}12 \text{ wt}\%$. Commonly, the
36 analysed melt inclusions have very high $\text{K}_2\text{O} (>6 \text{ wt}\%)$ and very low $\text{Na}_2\text{O} (<2 \text{ wt}\%)$
37 contents, indicative for potassic to ultrapotassic melts. Measured H_2O contents of the melts
38 range from 2.9 to 8.8 wt%, whereas CO_2 concentrations are between 160 and 1738 ppm.
39 Accordingly, calculated viscosities for re-homogenized melt inclusions vary between 10^4 and
40 $10^5 \text{ Pa}\cdot\text{s}$. Related primary fluid inclusions mainly contain CO_2 , with rare occurrence of CO
41 and N_2 , and are often associated with quartz, as well as different carbonates and
42 phyllosilicates. It is assumed that the source for the carbonic fluid was external and probably
43 related to the degassing lithospheric mantle. Consequently, it is argued that anatexis was
44 initially triggered by incongruent dehydration melting reactions involving biotite breakdown
45 and proceeded in the presence of an externally derived COH-bearing fluid. The coexistence
46 of COH-bearing fluid and melt inclusions indicates that partial melting occurred under

47 conditions of fluid-melt immiscibility. Potassic to ultrapotassic melt inclusions in UHT
48 granulites suggests that lower crustal anatexis may play a significant role in the redistribution
49 of heat-producing elements (such as K_2O), potentially influencing the thermal structure of the
50 continental crust.

51

52 **KEYWORDS:** Fluid inclusions; Garnet; Granites; Gruf Complex; Nanogranitoids

53

54 1. INTRODUCTION

55 Buoyant andesitic continental crust (e.g. Rudnick, 1995; Taylor & McLennan, 1985) is a
56 distinctive feature that differentiates the Earth from all the terrestrial planets of the Solar
57 System. Although the upper levels of continents can be easily studied and sampled, the
58 structure and chemical composition of the lower continental crust remain mostly enigmatic,
59 due to its inaccessibility for direct observations. Rock xenoliths entrained in lavas and
60 tectonically exposed metamorphic terranes, characterized by mineral assemblages that record
61 lower crustal pressures (i.e. 5-15 kbar), are the only opportunities to obtain useful
62 petrological information on the deep crust. A large number of such exposed terrains (e.g. the
63 Napier Complex in Antarctica, the Eastern Ghats granulite belt in India; see also Kelsey &
64 Hand, 2015) has provided a strong evidence that the lower continental crust can attain
65 extreme thermal regimes on a regional scale ($>775^\circ\text{C}/\text{GPa}$; e.g. Harley, 2008; Kelsey & Hand
66 2015; Brown & Johnson, 2018). Under these conditions, rocks are subjected to ultra-high
67 temperature (UHT) metamorphism, in which peak temperatures exceed 900°C at typical
68 pressures of 7-13 kbar (Harley, 1998), with important implications for the geochemical
69 differentiation, reworking and rheology of the continental lower crust (Brown, Korhonen, &
70 Siddoway, 2011; Jamieson, Unsworth, Harris, Rosenberg, & Schulmann, 2011). UHT
71 metamorphism is typically preserved in Mg-Al-rich metapelitic granulites (Brandt, Will, &

72 Klemm, 2007; Harley, Hensen, & Sheraton, 1990; Harley, 2008; Kelsey, 2008; Santosh,
73 Tsunogae, Li, & Liu, 2007), whose diagnostic paragenesis is characterized by the presence of
74 sapphirine+quartz, Al-rich orthopyroxene+sillimanite and osumilite-bearing mineral
75 assemblages (Harley, 1998; Kelsey, 2008). Progressing towards UHT conditions, the lower
76 crust buffers the increasing temperature undergoing extensive partial melting, with the
77 production of felsic magma that may then segregate from its source, leaving behind a more
78 mafic and less fertile residuum (Clemens & Stevens 2016; Sawyer 1994; Sawyer, Cesare, &
79 Brown, 2011; Vielzeuf & Holloway, 1988; White & Powell, 2002). Although S-type granites
80 and granitic leucosomes are the two most prominent products of crustal anatexis, they do not
81 provide the pristine chemical composition of the felsic anatectic melt because they are
82 affected by fractional crystallization, crystal accumulation, chemical contamination and
83 presence of xenocrysts (Carvalho, Sawyer, & Janasi 2016; Marchildon & Brown 2001;
84 Milord, Sawyer, & Brown, 2001; Sawyer, 2008; Sawyer et al., 2011; Stevens, Villaros, &
85 Moyen, 2007). Consequently, initial anatectic melt compositions have been mainly deduced
86 from experimental studies (e.g. Clemens, Holloway, & White, 1986; Le Breton & Thompson,
87 1988; Montel & Vielzeuf, 1997; Stevens, Clemens, & Droop, 1997) and thermodynamic
88 calculations (Grant, 2009; Holland & Powell, 2001; White, Stevens, & Johnson, 2011).
89 Another compelling method to determine the composition of crustal melts during the early
90 stages of anatexis is represented by the study of primary melt inclusions entrapped in
91 peritectic minerals during incongruent melting of metapelitic rocks (Acosta-Vigil, Cesare,
92 London, & Morgan, 2007; Acosta-Vigil et al., 2016; Bartoli et al., 2013; Bartoli, Acosta-
93 Vigil, Tajčmanová, Cesare, & Bodnar, 2016; Cesare, Marchesi, Hermann, & Gómez-
94 Pugnaire, 2003; Cesare, Ferrero, Salvioli-Mariani, Pedron, & Cavallo, 2009; Ferrero et al.,
95 2012; Ferrero, Wunder, Walczak, O'Brien, & Ziemann, 2015; Ferrero et al. 2019). Primary
96 melt inclusions (MI) in high-grade metamorphic rocks typically show variable degrees of

97 crystallization, ranging from glassy to fully crystallized, the latter also referred as
98 *nanogranitoids* (Cesare, Acosta-Vigil, Bartoli, & Ferrero, 2015). Since MI represent droplets
99 of an early crustal melt, they preserve precious information on its primordial composition,
100 before the melt is subjected to any chemical change due to magmatic differentiation.
101 At present, only few studies have approached a detailed investigation of primary melt and
102 fluid inclusions at, or near, UHT conditions (e.g. in the Kerala Khondalite Belt, Cesare et al.,
103 2009 and Ferrero et al., 2012, in the Athabasca granulite terrane, Tacchetto et al., 2019 or in
104 the Ivrea-Verbano Zone, Carvalho et al. 2019) and therefore the pristine composition of both
105 anatectic melts and fluids in UHT rocks is largely unconstrained. In order to overcome this
106 paucity, we examined primary melt and fluid inclusions in peritectic minerals observed in
107 UHT granulites of the Gruf Complex (Central Alps). The aim of this study is to provide a
108 microstructural framework and geochemical characterization of anatectic melts and fluids and
109 evaluate their role during crustal reworking processes associated to HT-UHT metamorphism.

110

111 **2. GEOLOGICAL SETTING**

112 The Penninic units of the Alpine nappe stack in the Central Alps are characterized by mineral
113 isograds, isotherms and isobars that have a concentric shape, defining the so-called
114 “Lepontine Metamorphic Dome” (Todd & Engi, 1997; Wenk, 1955). The Gruf Complex is a
115 ~12 x 10 km migmatitic body across Switzerland and northern Italy, located in the south-
116 eastern part of the Lepontine Dome (see Figure 1). To the west the Gruf Complex is
117 delimited by the Adula Nappe, whereas to the north is surrounded by the mafic-ultramafic
118 bodies of the Chiavenna Unit and by the crystalline rocks of the Tambo Nappe. To its eastern
119 and southern margin, the Gruf Complex is intruded by the Bergell pluton, a tonalitic to
120 granodioritic calc-alkaline intrusive body that formed between 33 and 30 Ma (Gianola et al.,
121 2014; Oberli, Meier, Berger, Rosenberg, & Gieré, 2004; Samperton et al., 2015; von

122 Blanckenburg, 1992). The southern extremity of the Gruf Complex, and part of the Bergell
123 intrusion, are then cut by the 24 Ma old Novate granite (Liati, Gebauer, & Fanning, 2000), a
124 strongly peraluminous S-type granitic stock composed by a swarm of dykes that presumably
125 derived from the partial melting of the surrounding gneissic units (von Blanckenburg, Früh-
126 Green, Diethelm, & Stille, 1992). The dominant lithologies of the Gruf Complex are
127 migmatitic orthogneisses, paragneisses and micaschists (Galli et al. 2011), which underwent
128 upper amphibolite facies migmatization (Bucher-Nurminen & Droop 1983; Nagel, De
129 Capitani, & Frey, 2002) between 34 and 29 Ma (Galli et al. 2012). These rocks are also
130 associated with irregular tabular bodies of charnockites and leucogranites (Galli et al. 2011).
131 Sapphirine-bearing granulites occur as schlieren in charnockites and as residual enclaves in
132 both migmatitic orthogneisses and charnockites (Galli et al. 2011). According to Galli et al.
133 (2011), granulites and charnockites formed at ultra-high temperature conditions of $T = 920-$
134 940°C and $P = 8.5-9.5$ kbar, while migmatization of the surrounding gneissic and metapelitic
135 lithologies took place at $\sim 740^{\circ}\text{C}$ and $6.5-7.5$ kbar (Galli, Le Bayon, Schmidt, Burg, &
136 Reusser, 2013).

137

138 3. ANALYTICAL TECHNIQUES AND EXPERIMENTAL METHODS

139

140 Back-scattered electron (BSE) images and semi-quantitative energy dispersive spectroscopy
141 (EDS) analyses of MI were carried out with a CamScan MX2500 Scanning Electron
142 Microscope (SEM), at the Department of Geosciences of the University of Padova (Italy).
143 Micro-Raman spectroscopy of MI was conducted with a HORIBA Jobin-Yvon LabRAM HR
144 800, equipped with a Nd:YAG laser ($\lambda = 532$ nm, laser power on sample $\sim 2-3$ mW), at the
145 Institute of Earth and Environmental Science, University of Potsdam. Raman spectra were
146 acquired between 100 and 4000 cm^{-1} with an acquisition time of 20 s during three spectral

147 accumulations. The typical setup also included a grating of 300 lines/mm, a slit width of 100
148 μm and a confocal hole set at 200. Spectral resolution is considered to be of $\sim 10\text{ cm}^{-1}$,
149 compared to available literature and databases.

150 The chemical composition of garnet was measured with a CAMECA SX50 electron
151 microprobe (EPMA), equipped with four wavelength dispersive spectrometers (WDS), at the
152 C.N.R.-I.G.G. (Consiglio Nazionale delle Ricerche – Istituto di Geoscienze e Georisorse),
153 Department of Geosciences, University of Padova. Analyses were carried out using a
154 focussed beam with a current of 20 nA and an accelerating voltage of 15 kV. Counting times
155 for each element were 10 s on peak and 5 s for the background.

156 Major element composition of glass and minerals in the re-homogenized and glassy MI were
157 determined with a JEOL JXA-8200 Superprobe, equipped with five WDS, at the Department
158 of Earth Sciences (University of Milano, Italy), employing an acceleration voltage of 15 kV,
159 a beam current of 5 nA and beam diameter of 1 μm . Acquisition times were 10 s on peak and
160 5 s for background, measuring Na and K first to avoid diffusional losses. Alkali
161 concentrations were corrected using conservative factors obtained by the analysis of hydrous
162 and anhydrous leucogranitic glasses of known composition. In particular, the standards
163 employed in this study were a 10.1 wt% H_2O -bearing glass (LGB 2; Behrens & Jantos,
164 2001), a 5.5 wt% H_2O -bearing glass (DL; Acosta-Vigil, London, Morgan, & Dewers, 2003)
165 and a nearly anhydrous ($\text{H}_2\text{O} = 300 \pm 42\text{ ppm}$) glass (B; Morgan & London, 2005).

166 Single garnet core and rim fragments ($\sim 1.5 \times 2\text{ mm}$ in size), used for the re-homogenization
167 experiments of the nanogranitoids, were manually separated by cutting from 1.5 mm-thick
168 double-polished thick sections. Two sets of experiments were performed. In the first set,
169 garnet chips were charged into Au capsules (external and internal diameter of 3 mm and 2.7
170 mm, respectively) alternating them with powdered graphite (granulometry $< 45\text{ }\mu\text{m}$). In the
171 second type of experiments, the same gold capsules were filled with alternating layers of

172 garnet chips and powdered SiO₂, obtained from tetraethylorthosilicate (TEOS). In both cases,
173 capsules were crimped and sealed with an arc-welder. Experiments with garnet+graphite
174 charges were conducted using a single-stage and an end-loaded piston cylinder apparatuses at
175 the Laboratory of Experimental Petrology, Department of Earth Sciences, University of
176 Milano. Capsules were placed vertically into MgO spacers and then inserted in a NaCl
177 sleeve-pyrex (only for end-loaded piston cylinder)-graphite piston cylinder assembly. The
178 temperature was monitored by a K-type (nickel-chromium / nickel-alumel) thermocouple,
179 with an estimated accuracy of $\pm 5^{\circ}\text{C}$ and no corrections for the pressure effects on the
180 electromotive force were applied. Experiments were performed at 10-12 kbar (i.e. higher than
181 the calculated peak conditions, in order to prevent decrepitation of the inclusions) between
182 950°C and 800°C and with variable run durations (from 1 to 10 hours). This allowed to
183 constrain the interval in which re-homogenization was best attained. All runs were first
184 pressurized to 10-12 kbar at room temperature and then the assembly was isobarically heated
185 at a constant heating rate ($100^{\circ}\text{C}/\text{min}$) until the targeted temperature was achieved. The
186 experiments were terminated by switching off the power supply, resulting in quenching rates
187 of $\sim 40^{\circ}\text{C}/\text{s}$. Capsules were then dissolved in aqua regia and the recovered garnets were
188 singularly mounted in epoxy resin. Experiments with garnets+quartz charges were performed
189 at the Institute of Geochemistry and Petrology, ETH Zurich, using a single stage and an end-
190 loaded piston cylinder apparatuses. The assembly consisted of a talc sleeve, pyrex (only for
191 end-loaded piston cylinder), a graphite furnace and MgO spacers, in which the Au capsules
192 were positioned. Temperature was measured by a B-type (Pt₉₄Rh₆-Pt₇₀Rh₃₀) thermocouple
193 (accuracy: $\pm 5^{\circ}\text{C}$). Experiments were performed at 12 kbar, 875°C and with a run duration of
194 10 h. The experimental procedure was the same used for the experiments with
195 garnets+graphite charges. Although the two set of experiments were performed in slightly

196 different assemblies, it is assumed that this has no relevant influence on the re-
197 homogenization of the inclusions.

198 H₂O and CO₂ contents of remelted inclusions were determined by Nano Secondary Ion Mass
199 Spectrometry (NanoSIMS) employing a Cameca NanoSIMS 50 at Muséum National
200 d'Histoire Naturelle of Paris, following the approaches of Bartoli, Cesare, Remusat, Acosta-
201 Vigil, and Poli (2014) and Créon, Levresse, Remusat, Bureau, and Carrasco-Núñez (2018).

202 Polished experimental capsules with quartz-garnet charges and standard glasses were
203 mounted in indium to lower the hydrogen background in the analysis chamber (Aubaud et al.,
204 2007), and coated with gold (20 nm thick). Before each analysis, a 5 x 5 µm surface area was
205 initially pre-sputtered for 150 s with a 170 pA primary Cs⁺ rastering beam, in order to remove
206 the gold coating and reach a sputtering steady-state (Thomen, Robert, & Remusat, 2014).

207 Subsequently, the primary Cs⁺ beam was set at 17 pA and scanned over a surface area of 3 x
208 3 µm. Nevertheless, to avoid surface contamination, only ions from the inner 1 x 1 µm region
209 were collected with the “beam blanking mode”. Exposed MI were analysed through
210 collection of secondary ions of ¹²C⁻, ¹⁶OH⁻, ²⁸Si⁻ and ⁵⁶Fe¹⁶O⁻ in multicollection mode. Mass
211 resolving power was set at minimum 5500, enough to resolve interferences on ¹⁶OH⁻. Each
212 analysis consisted in a stack of 200 cycles, with a duration of 1.024 s for every single cycle.

213 The vacuum in the analysis chamber never exceeded 2.5 x 10⁻¹⁰ Torr during the entire session
214 of measurements. H₂O and CO₂ contents of the glasses were quantified measuring ¹⁶OH⁻/²⁸Si⁻
215 and ¹²C⁻/²⁸Si⁻ ratios, respectively (Bartoli et al., 2014; Créon et al., 2018). These ratios were
216 converted into concentrations using calibration curves obtained from standards of known
217 composition. Standards for the determination of H₂O included two standards used for the
218 alkali correction (DL and B, see above) plus an additional hydrous glass with 4.3 wt% H₂O
219 (LGB1; Behrens & Jantos, 2001). On the other hand, standards for CO₂ consisted in four
220 trachyandesites (STR 9, 10, 11 and 13) from the Stromboli volcano, experimentally doped in

221 carbon and water by Bureau et al. (2003). Concentrations and uncertainties were calculated
222 using the R program, following the procedure described in Bartoli et al. (2014) and Thomen
223 et al. (2014). Average major element and volatile concentrations of the analysed MI are
224 reported in Table 1.

225

226 **4. RESULTS**

227

228 **4.1 Mineral assemblages of the UHT granulites**

229 All the investigated samples were collected in the lower part of Val Codera, near the locality
230 of Bresciadega (see also Galli et al., 2011). Two varieties of UHT granulite with granofelsic
231 texture were studied (Figure 2). The first type corresponds to type A of Galli et al. (2011) and
232 consists of a dark, massive granulite containing up to 2 cm large garnet (Grt) and up to 5 mm
233 sapphirine (Spr) porphyroblasts, associated with a matrix of up to 3 mm-sized orthopyroxene
234 (Opx), cordierite (Crd), biotite (Bt) and K-feldspar (Kfs). Garnet appears as faint pink,
235 rounded crystals showing a clear zonation. Numerous mineral inclusions of biotite,
236 orthopyroxene, sapphirine, plagioclase (Pl), cordierite, rutile (Rt), ilmenite, sillimanite,
237 tourmaline, apatite (Ap), spinel, staurolite, corundum, monazite and zircon are present within
238 the porphyroblastic garnets. On the other hand, sapphirine is generally hypidiomorphic,
239 prismatic and pleochroic (from pale-red to blue), showing sometimes a longitudinal, simple
240 twinning system.

241 The second type of granulite belongs to type C of Galli et al. (2011). The rock is massive and
242 melanocratic with a mineral assemblage made of up to 1.5 cm large porphyroblastic garnet,
243 porphyroblastic orthopyroxene (<1.5 mm), biotite, cordierite, sillimanite and symplectitic
244 spinel. Sapphirine may be present as symplectitic grains in the rock matrix, or as small (<500
245 μm) inclusions within garnet. Other mineral inclusions observed within garnet grains are:

246 biotite, quartz, sillimanite, cordierite, plagioclase, spinel, zircon, apatite, corundum, rutile,
247 staurolite and tourmaline.

248 In both granulites, melt inclusions (MI) are mainly present in the porphyroblastic garnets,
249 where they may occur as single, scattered inclusions or may form mm-large clusters. These
250 clusters are commonly found in the cores of the garnets (Figure 3a,b), but their occurrence
251 towards to the rims has been also noticed (Figure 3c,d). The presence of different birefringent
252 crystals under crossed polars (Figure 3e,f) indicates that the majority of MI are
253 polycrystalline (i.e. nanogranitoids; Cesare et al. 2015). Often, fluid inclusions occur
254 associated to nanogranitoids within the same clusters. Typically, fluid inclusions show a
255 distinctive darker appearance and high birefringence (Figure 3g). Moreover, sporadic glassy
256 inclusions containing shrinkage bubbles have been also observed (Figure 3h). In contrast to
257 polycrystalline MI, glassy MI occur exclusively as single inclusions dispersed in the garnets,
258 without forming clusters. Occasionally, glassy MI may occur also close to nanogranitoids. MI
259 with multiple birefringent phases have been also identified in sapphirine porphyroblasts of
260 Type A granulites (Figure 3i). The MI in sapphirine are too rare to allow their experimental
261 re-melting, but they were characterized by Raman spectroscopy.

262

263 **4.2 Micro-Raman characterization of glassy, nanogranitoid and fluid inclusions**

264 Micro-Raman investigations for the glassy inclusions observed in Type A samples show that
265 the glass is hydrous (see Figure 4a). Furthermore, the single Raman band displayed at 1382
266 cm^{-1} (Figure 4a) indicates that some dissolved molecular CO_2 is also present in the melt
267 (Brooker, Kohn, Holloway, McMillan & Carroll, 1999; Ni & Keppler 2013). Shrinkage
268 bubbles in the glass contain CO_2 , as demonstrated by the presence of the “Fermi-doublet” in
269 the Raman spectra (see Figure 4a). Densities of CO_2 in these bubbles (see Table S1),
270 calculated with the densimeter of Wang et al. (2011), range between 0.5 and 0.8 g/cm^3 (± 0.3

271 g/cm³). Raman analyses showed that nanogranitoids (Figure 4b,c) contain quartz, muscovite,
272 phlogopite, K-feldspar, kokchetavite (a polymorph of KAlSi₃O₈) and an unknown phase with
273 a main Raman peak at 430 cm⁻¹. A phase with identical spectrum has been identified in
274 nanogranitoids from other case studies and it is currently under investigation (Ferrero,
275 unpublished data). Unexpectedly, Raman investigations also showed that some of these
276 nanogranitoids could retain some CO₂ bubbles (Figure 4b,c), suggesting the existence of
277 micropores. Nanogranitoids observed in sapphirine crystals from type A granulites (Figure
278 4d) contain quartz, muscovite, kokchetavite and the same unknown phase with the peak at
279 430 cm⁻¹.

280 Fluid inclusions (FI), present in both granulites, display a fluid fraction as well as a solid
281 portion, in which several phases were identified. In type A granulites muscovite, Fe-
282 magnesite, calcite, pyrophyllite, quartz and biotite were the most common phases, besides
283 CO₂. FI in type C granulites, in addition to the same phases observed for type A, have
284 paragonite, magnesite, siderite, phlogopite, N₂ and CO (Figure 4e,f). For one inclusion it was
285 possible to calculate the relative amount of components in the fluid, applying the method of
286 Dubessy, Poty, and Ramboz (1989). The obtained molar fractions were 94 mol% for CO₂ and
287 6 mol% for N₂. Regarding the carbonate phases, Fe-magnesite in FI of both granulites has
288 variable Fe content ($Fe\# = 100 \times Fe/(Fe+Mg+Mn+Ca+Al)$), as defined by Boulard, Guyot, &
289 Fiquet, 2012), typically ranging between $Fe\# = 20$ and $Fe\# = 55$. Calculated CO₂ densities
290 (Wang et al. 2011) for FI in type A granulites vary between 0.3 and 1.0 g/cm³ (see Table S1),
291 a range comparable to that calculated for type C granulites (0.4-0.8 g/cm³). Remarkably,
292 neither in the shrinkage bubbles of glassy inclusions nor in fluid inclusions, H₂O was
293 detected.

294

295

296 **4.3 Microstructures of nanogranitoids**

297 Detailed observations by SEM allowed to determine the principal microstructural features of
298 nanogranitoids, as well as their mineral assemblage. Typically, MI of both Type A and C
299 granulites have an elliptical faceted shape, with major axes ranging between 2 and 115 μm
300 (Figure 5a-f). Nevertheless, for Type A, the size of MI decreases from rims to cores. MI in
301 the rims have an average size of $47 \pm 5 \mu\text{m}$, those found in the intermediate region of the
302 garnets (i.e. between cores and rims) are $35 \pm 5 \mu\text{m}$, while MI found in the cores have an
303 average size of $24 \pm 3 \mu\text{m}$. Together with nanogranitoids with a nearly negative crystal shape
304 (Figure 5a,b), some MI display natural decrepitation, with offshoots that are arranged radially
305 around the inclusions (Figure 5c,d). The number of offshoots per inclusion varies drastically
306 (from 1 to 10), with larger inclusions showing more and usually longer offshoots. The
307 calculated average length of the offshoots for MI $<45 \mu\text{m}$ in size is $6 \mu\text{m}$, whereas MI bigger
308 than $45 \mu\text{m}$ have an average length of the offshoots of $13 \mu\text{m}$. Glassy inclusions in Type A
309 granulites show negative crystal shapes and their size is $<15 \mu\text{m}$, with an average diameter of
310 $8 \mu\text{m}$. MI in type C granulites also have an elliptical faceted shape and show a polycrystalline
311 nature. However, in contrast to MI in type A granulites, they have similar sizes from core to
312 rim and hardly exceed $40 \mu\text{m}$ in diameter, with an average length of the major axis of 21 ± 2
313 μm . Also garnets from type C granulites show some decrepitated MI (Figure 5e,f), which
314 have an average length of the offshoots of $5 \mu\text{m}$.

315 In general, the mineral assemblage within nanogranitoids has an inequigranular and
316 interlobate fabric composed of mainly hypidiomorphic crystals of quartz, biotite, muscovite,
317 plagioclase, K-feldspar and very rarely aluminosilicates (Figure 5a-f). Sometimes
318 nanogranitoids clearly display an igneous microstructure defined by intergrowths of quartz,
319 feldspars and biotite (Figure 5e-f). SEM analyses also highlighted the presence of accessory

320 minerals, typically Cl-bearing apatite and rutile, which are usually more idiomorphic
 321 compared to the other phases (Figure 5d,e).

322

323 **4.4 Chemical composition of host garnets and minerals in nanogranitoids**

324 In this section we report only chemical analyses of garnet porphyroblasts. For detailed
 325 chemical analyses of all rock-forming minerals see Galli et al. (2011). Analysed garnets of
 326 Type A and Type C granulites are almost pure almandine-pyrope solid solutions (see Table
 327 S2 and Figure S1) and display a zonation marked by pyrope-richer rims (Type A = Alm₄₀₋
 328 ₅₂Prp₄₃₋₅₅Sps₀₋₂Grs₂₋₆; Type C = Alm₄₆₋₅₄Prp₄₃₋₅₂Sps₀₋₁Grs₁₋₃) compared to cores (Type A =
 329 Alm₄₈₋₆₁Prp₂₆₋₄₆Sps₁₋₄Grs₃₋₁₂; Type C = Alm₅₃₋₆₂Prp₃₂₋₄₃Sps₀₋₁Grs₃₋₆). Nevertheless, Type C
 330 granulites may also have garnets with cores enriched in pyrope-component (Alm₄₁₋₄₈Prp₄₈₋
 331 ₅₇Sps₀₋₁Grs₂₋₄) compared to rims (Alm₄₂₋₅₃Prp₄₃₋₅₄Sps₀₋₁Grs₂₋₄).

332 Nanogranitoids are often too small to allow a precise chemical characterization of their
 333 mineral assemblage. Nevertheless, some nanogranitoid inclusions in Type A granulites were
 334 large enough and their single mineral phases were measured (see Table S3). Plagioclases
 335 show variable X_{An} [$An/(An+Ab)$] between 0.10 (albite) and 0.49 (andesine). By contrast,
 336 biotites are Ti-free and characterized by X_{Mg} [$Mg/(Mg+Fe^{2+})$] ranging from 0.71 to 0.86.
 337 Other K-rich phases that have been recognized are K-feldspar and white mica, the latter
 338 displaying a $X_{Mg} = 0.59$.

339

340 **4.5 Remelted nanogranitoids**

341 Experiments between 900 and 875°C produced the most homogenized glasses. Remelted MI
 342 are typically <15 µm in size and display elongated to perfect negative crystal shapes (Figure
 343 6a-d). Some inclusions, together with glass, display mineral phases such as rutile and apatite
 344 that indent the walls of the MI (Figure 6c). These phases are interpreted to be accidental

345 minerals trapped during the formation of the inclusions, since they are observed before and
346 after the re-homogenization experiments. Therefore, they are not daughter minerals (i.e.
347 phases that crystallized directly from the melt; e.g. Ferrero et al., 2012; Acosta-Vigil et al.
348 2016). Moreover, few MI may also exhibit bubbles (Figure 6d), suggesting that the fluid
349 underwent incomplete dissolution in the melt during the experimental run or, alternatively, it
350 diffused during cooling to form shrinkage bubbles (Lowenstern, 1995). A little fraction of the
351 analysed MI population is characterized by the presence of unmelted daughter minerals,
352 testifying incomplete remelting (Figure 6e,f). Typical daughter minerals coexisting with glass
353 are euhedral to subhedral biotite grains ($X_{Mg} = 0.82-0.88$ and $TiO_2 < 0.2$ wt%, see Table S4)
354 and rounded quartz crystals.

355 Experiments with garnets+quartz charges at 875°C produced substantial amounts of melt in
356 the matrix outside the garnets (Figure 6g). This melt infiltrated within the garnet crystals and
357 led to the formation of large melt pockets. The latter ones differ microstructurally from
358 remelted MI by their size (commonly >20 μm in diameter, although few of them have sizes
359 comparable to remelted MI) and by the striking abundance of bubbles, a feature that indicates
360 high fluid contents (Figure 6h). The matrix melt derives from the melting of mineral
361 intergrowths or matrix phases, such as biotite and feldspar, which could not be avoided
362 during the manual crushing of the garnet chips. Often, a peritectic reaction between the melt
363 and the garnet produced orthopyroxene or corundum (Figure 6g).

364 Evidence of overheating in the MI during experiments has been observed at all temperatures,
365 but predominantly at 950°C. This is indicated by the interaction between melt and garnet,
366 with the formation of peritectic phases such as orthopyroxene (Figure 6i) or gedrite, the
367 recrystallization of new garnet within the inclusion or changes in the chemical composition of
368 the garnet around the remelted inclusions. Chemical analyses of peritectic orthopyroxenes
369 (see Table S4) indicate that they are Al-rich (8.3-10.4 wt% at 950°C and 6.5-9.2 wt% Al_2O_3

370 at lower temperature), with $X_{Mg} = 0.69-0.73$ (at 950°C) and 0.67-0.84 (at 900-875°C). These
371 compositions are comparable to those measured in the orthopyroxene porphyroblasts in the
372 matrix of the granulites (Galli et al. 2011). One analysis of a recrystallized garnet at 950°C
373 shows that the new garnet is Fe-poorer and Mg-richer ($X_{Mg} = 0.64$) compared to the original
374 garnet composition ($X_{Mg} = 0.47$). Since at 950°C microstructural evidence for overheating is
375 dominant, the glasses analysed at these conditions were considered not representative and
376 therefore disregarded (Figure S2). In the experiments performed at 800°C, MI often display
377 incomplete remelting and only rare homogeneous glasses could be found. This might indicate
378 that this temperature corresponds to the lower boundary for remelting experiments.

379

380 **4.6 Chemical composition of glasses**

381 Figure 7a-b and Table S5 report chemical analyses of glasses for remelted inclusions and for
382 preserved glassy inclusions, all recalculated on anhydrous basis. For what concerns
383 experimentally remelted MI, analyses that displayed clear evidence for
384 contamination/interaction with the host garnet, or mixing with matrix melt, were discarded
385 and are not further discussed (see Figure S2). Glasses are dominantly peraluminous ($ASI =$
386 $1.0-1.6$, $[Al_2O_3/(CaO+Na_2O+K_2O)]_{molar}$), with only one MI that falls into the peralkaline
387 field. Natural glassy inclusions have a slightly more restricted range ($ASI = 1.0-1.1$)
388 compared to re-homogenized nanogranitoids. With some exceptions, analysed MI are
389 corundum-normative ($Crn = 0.20-4.88$, see Table S5). Both re-homogenized MI and glassy
390 inclusions are predominantly rhyolitic in composition, with $SiO_2 = 68.6-79.7$ wt% and
391 $Na_2O+K_2O = 5.3-12.0$ wt% (on anhydrous basis), developing a negative correlated trend in
392 the SiO_2 vs. Na_2O+K_2O space (Figure 7b). However, melts with a trachytic composition have
393 been also observed, as shown by one MI from Type A granulite remelted at 875°C. Glassy
394 inclusions have slightly higher total alkali contents compared to remelted nanogranitoids.

395 Plotted in Harker variation diagrams (Figure 8 a-f), glassy and re-homogenized inclusions
396 show a clear increase in Al_2O_3 and K_2O with decreasing SiO_2 . By contrast, CaO ,
397 $\text{FeO}+\text{MgO}+\text{TiO}_2$, Na_2O and Cl display more scattered distributions. Glassy inclusions differ
398 from re-homogenized nanogranitoids by their low CaO (<0.2 wt% vs. 0.2-2.0 wt%) and
399 $\text{FeO}+\text{MgO}+\text{TiO}_2$ (<1.4 wt% vs. 1.4-3.4 wt%) concentrations. All the analysed melt
400 inclusions are characterized by a decoupling in the alkali content, with most inclusions
401 showing Na_2O concentrations <2 wt% and K_2O >6 wt%. Re-homogenized MI have variable
402 $\text{K}\#$ ratios [$\text{K}\# = \text{molar K}_2\text{O}/(\text{K}_2\text{O}+\text{Na}_2\text{O}) \times 100$], ranging from 72 to 99 (average: 87 ± 4) for
403 Type C granulites and from 56 to 82 (average: 71 ± 8) for Type A granulites. Similarly,
404 glassy inclusions from Type A granulites have $\text{K}\#$ between 59 and 87 (average: 77 ± 5).
405 H_2O and CO_2 concentrations of remelted inclusions, determined by NanoSIMS, are reported
406 in Table 2 and shown in Figure 9. H_2O contents in the analysed MI range from 2.9 to 8.8
407 wt%, without any clear distinction between garnet cores and rims. Indeed, calculated
408 averages are 6.2 ± 1.3 wt% (type A) and 7.1 ± 3.0 wt% (type C) for garnet cores, whereas for
409 garnet rims is 4.4 ± 0.9 (type C). By contrast, CO_2 concentrations allow to subdivide the
410 analysed MI into two distinct families, one clustering at ~ 1200 ppm and the other showing
411 concentrations <500 ppm. From Figure 9 it is also possible to notice that MI with low CO_2
412 concentrations are characterized by a narrower range in H_2O (4.1-5.5 wt%) compared to MI
413 with higher CO_2 contents.

414

415 **5 DISCUSSION**

416 **5.1 Anatexis close to UHT conditions**

417 The mineral assemblage displayed by nanogranitoid inclusions within the peritectic garnet of
418 the studied granulites indicates that these inclusions represent droplets of pristine felsic melt,
419 an observation that was also confirmed by the measurement of their chemical composition

420 after remelting experiments. As suggested by Galli et al. (2011) garnet porphyroblasts are
421 peritectic minerals generated by fluid-absent biotite melting along the prograde heating stage.
422 Further investigations of Guevara and Caddick (2016) and Oalman, Duesterhoeft, Möller,
423 and Bousquet (2019) by means of phase equilibria modelling, showed that garnet in the Gruf
424 granulites grows along the up-temperature path and then starts to be consumed at ~920-950
425 °C. It follows that MI experimentally re-homogenized at 875-900 °C were trapped while
426 garnet was growing along the prograde heating path. Therefore, the investigated MI allow an
427 appraisal of crustal melts and anatexis near to UHT conditions.

428 Granulites from the Gruf Complex are characterized by the presence of glassy and
429 nanogranitoid inclusions. Their coexistence at the micrometric scale indicates that the melt
430 behaves differently when it is trapped within pores. Glassy inclusions are on average smaller
431 than nanogranitoids and therefore their preservation may be explained by inhibition of
432 crystallization (Cesare et al., 2009) due to the greater supersaturation required by smaller
433 pores to develop crystals compared to larger ones (Holness & Sawyer, 2008). Alternatively,
434 lower H₂O contents and, in turn, higher viscosities in some inclusions could have inhibited
435 the nucleation with the formation of glass (Bartoli, Acosta-Vigil, & Cesare, 2015). A
436 different volatile content in glassy and crystallized melt inclusions seems to be supported by
437 the different electron microprobe totals (Table 1). MI display compositional trends in SiO₂
438 and total alkali that may be ascribed to local diffusion in the melt (Acosta-Vigil et al., 2017)
439 or due to lack of melt interconnection (Bartoli et al., 2019). In general, the chemical
440 composition of re-homogenized MI is consistent with the mineral assemblage observed in the
441 nanogranitoids. This can be also observed in the AKF diagram (Figure 10), where analysed
442 glasses for Type A granulites plot within the triangle defined by the tie-lines of the minerals
443 measured in the non-remelted nanogranitoids. Although the chemical composition of the
444 minerals forming MI in Type C granulites could not be measured (Figure 10b), it is assumed

445 that the mineral assemblage should be similar to the one noticed for Type A granulites and
446 therefore an equivalent triangle for MI in Type C granulites is expected. From Figure 10a it is
447 also possible to observe that glassy inclusions plot towards the K-apex of the triangle, while
448 remelted MI tend to be more scattered, with some analyses plotting slightly outside the
449 triangle defined by the mineral assemblage. In the Qz-Ab-Or normative diagram (see Figure
450 S3) glassy and re-homogenized inclusions from the Gruf Complex plot close to the Qz-Or
451 join, considerably away from the haplogranite ternary eutectic. Furthermore, MI also plot at
452 lower Ab-contents compared to charnockites, leucogranites and S- and A-type granites, but
453 overlap the field displayed by MI from the Kerala Khondalite Belt.

454 Figure 8 shows that the analysed glasses have markedly different compositions compared to
455 the charnockites of the Gruf Complex (see Galli et al., 2013), indicating that the charnockites
456 might have been generated from another metapelitic source or during a melting event
457 unrelated with the formation of the granulites. Alternatively, charnockites do not represent
458 true primary melt compositions as expected in rocks crystallized at lower crustal conditions
459 and/or are slightly modified by the entrainment of peritectic phases such as garnet and
460 orthopyroxene. By contrast, MI have similar concentrations for CaO, Al₂O₃ and
461 FeO+MgO+TiO₂ compared to the leucogranites that intrude the migmatitic paragneisses and
462 micaschists (Galli et al. 2013). Moreover, MI overlap the trend displayed by the melt
463 inclusions from the Kerala Khondalite Belt (Cesare et al. 2009; Ferrero et al. 2012), even
464 though the latter have slightly higher FeO+MgO+TiO₂ and Cl concentrations. On the other
465 hand, MI from the Gruf Complex have different trends for FeO+MgO+TiO₂, alkalis, and
466 partly CaO, compared to A- and S-type granites. This evidence strongly reinforces the
467 assumption that S- and A-type granites, similar to the Gruf charnockites, do not mirror
468 primary crustal melts, but liquids modified by a large plethora of mechanisms during their
469 production and segregation from the source (see INTRODUCTION).

470 MI are characterized by high K_2O and low Na_2O concentrations compared to regional
471 charnockites and leucogranites, but also relative to A- and S-type granites (Figure 8d-e).
472 However, a decoupled behaviour in alkali contents has been also noticed in the MI from the
473 Kerala Khondalite Belt (KKB, S-India), in which ultrapotassic rhyolitic melts have been
474 reported (Cesare et al. 2009; Ferrero et al., 2012). It is generally believed that khondalites
475 from the KKB originated during crustal anatexis at UHT conditions (Nandakumar and
476 Harley, 2000; Yu, Santosh, Li, & Shaji, 2019) and therefore it seems that high K_2O/Na_2O
477 ratios are a distinctive feature of anatectic melts at extremely high crustal temperatures. K-
478 rich melts have also been experimentally derived by Patiño Douce and Johnston (1991) from
479 a pelitic starting material. In particular, their experiments between $P = 7-13$ kbar and $T =$
480 $875-1075^\circ C$ give K_2O -rich and Na_2O -poor liquids that closely resemble MI from the Gruf
481 Complex and the KKB. Additionally, Droop, Clemens, & Dalrymple (2003) obtained K-rich
482 melts ($K_2O/Na_2O = 4.1-9.5$) from partial melting experiments of metapelitic micaschists at
483 $900^\circ C$ and 5 kbar.

484 In the AKF diagram (Figure 10), analyses for the KKB, as well as the experimental glasses of
485 Droop et al. (2003) and Patiño-Douce & Johnston (1991), plot towards the K-apex,
486 overlapping in part the field formed by the MI of the Gruf Complex. The fact that K-rich
487 melts are observed up to UHT conditions, independently of the pressure, may be explained by
488 the role of titanium and other elements such as F, Cl and Fe^{3+} in expanding the stability field
489 of biotite towards higher temperatures (e.g. Mouri, Guiraud, & Hensen, 1996; Stevens et al.,
490 1997; Tajčmanová, Connolly, & Cesare, 2009). Consequently, the melting of biotite may be
491 delayed, compared to the melting of sodic plagioclase, leading to an enrichment of potassium
492 in the melt.

493 All this evidence suggests that crustal melts produced at the onset of anatexis under high to
494 ultra-high temperature conditions are dominantly potassic to ultrapotassic, as was also
495 recognized in previous studies (Cesare et al., 2009; Ferrero et al., 2012).

496

497 **5.2 Volatiles in the deep crust**

498 Primary clusters of melt and fluid inclusions occur typically in both garnet cores and rims of
499 the granulites from the Gruf Complex, indicating that they were entrapped during the same
500 anatectic event. The coexistence of CO₂ with stepdaughter phases such as carbonates (Fe-
501 magnesite, siderite and calcite) and phyllosilicates (e.g. pyrophyllite, muscovite and biotite)
502 within FI strongly suggests that the original fluid had a COH(N) composition. Nevertheless,
503 the presence of K-rich phases such as muscovite and biotite might also indicate that some of
504 the FI are instead mixed inclusions (fluid+melt) and therefore part of the H₂O may derive
505 from the melt. Similar mixed inclusions were documented in garnet of crustal enclaves
506 (Cesare, Maineri, Baron Toaldo, Pedron, & Acosta-Vigil, 2007), in anatectic granitoids
507 (Ferrero, Braga, Berkesi, Cesare, & Laridhi Ouazaa, 2014) and in low-to-medium pressure
508 migmatites (Ferrero, Wunder, Ziemann, Wälle, & O'Brien, 2016). Although H₂O as a free
509 phase has never been demonstrated by Raman spectroscopy within the measured FI of the
510 Gruf Complex, its occurrence at the nanometric scale cannot be excluded (see also Lamadrid,
511 Lamb, Santosh, & Bodnar, 2014; Esposito et al., 2016). On the other hand, carbonates and
512 phyllosilicates are interpreted as re-speciation products after post-entrapment carbonation and
513 hydration reactions between garnet host and fluid, as it has been suggested also for other
514 HT/UHT terranes (Ferrero et al. 2014; Tacchetto et al., 2019; Carvalho et al., 2019, 2020).
515 Hence, the different densities displayed by the FI are a direct consequence of incomplete
516 reactions, which leave a variable amount of CO₂ in the residual fluid.

517 Raman spectroscopy measurements allowed to confirm the presence of CO₂ and H₂O in
518 glassy and nanogranitoid inclusions (see Fig. 4), indicating that both types of inclusions
519 derived from the similar melt. The ubiquity of pure CO₂-rich shrinkage bubbles (without any
520 apparent detectable H₂O, see discussion above) within glassy inclusions can be explained by
521 the preferential partition of H₂O into silicate melt than CO₂ (e.g. Holtz, Johannes, Tamic, &
522 Behrens, 2001; Tamic, Behrens, & Holtz, 2001). Further investigations by NanoSIMS
523 enabled the quantification of the minimum volatile component dissolved in this melt. The
524 dissolved H₂O measured in the MI displays a wide spectrum between 2.9 and 8.8 wt%, with a
525 large proportion of the analyses that have >5 wt%. Such values indicate that crustal melts at T
526 ~900°C can have higher H₂O contents than commonly assumed for the haplogranitic system.
527 However, as pointed out by Holtz et al. (2001), this behaviour is to be expected for melts that
528 markedly differ from eutectic compositions and that involve the breakdown of micas in the
529 melting reaction, conditions which are both realised for the MI from the Gruf Complex.
530 Moreover, analogous H₂O contents have been also observed in MI from the granulites and
531 upper amphibolite-facies migmatites from the Strona Valley, in the Ivrea Zone (Carvalho et
532 al., 2019). This may suggest that, at HT/UHT conditions, anatectic rhyolitic melts have
533 considerable but uneven H₂O contents, which may strongly affect the viscosity and therefore
534 the mobility of these magmas. Variable H₂O contents in anatectic melts were also recognized
535 by Bartoli et al. (2014) in peritectic garnets of amphibolite-facies migmatites close to the
536 Ronda peridotite and were interpreted to represent micro-scale buffered compositions due to
537 heterogeneous domains in the precursor. A similar mechanism might be envisaged also for
538 the MI of the Gruf Complex, since low and high values sometimes can be found in the same
539 garnet crystal. Another striking feature of the analysed MI is the marked difference in the
540 CO₂ contents (Figure 9). MI form two distinct groups, with the highest CO₂ concentrations

541 that are nearly identical to those observed in MI from granulites and amphibolites from the
542 Ivrea Zone (see also Carvalho et al., 2019).

543 Our results clearly demonstrate that the peritectic garnets of the investigated UHT granulites
544 grew with coexisting COH-bearing fluids and silicate melts, that, due to the low solubility of
545 CO₂ in silicate melts (Holtz et al., 2001; Tamic et al., 2001), led to fluid-melt immiscibility.

546 The origin of the COH fluid in high-grade metamorphic rocks is source of debates. The
547 granulites from the Gruf Complex lack graphite in their mineral assemblage and therefore an
548 internal origin for carbon seems to be unlikely. However, the absence of graphite in the rocks
549 does not preclude the possibility that graphite was present in the original mineral assemblage
550 and was completely consumed before or during anatexis. Another source for carbon may be
551 represented by carbonaceous sediments interlayered in metapelitic rocks. In the Gruf
552 Complex, rare, up to 20 x 1 meter lenses of calc-silicates occur all along the contact with the
553 Bergell tonalite, but never within the migmatitic gneisses that host the UHT granulites (Galli
554 et al., 2013). Furthermore, scarce, up to 20-meter-thick discontinuous bands of calc-silicates
555 have been only recognized in the mafic-ultramafic Chiavenna Unit adjacent to the Gruf
556 Complex (Schmutz, 1976). Thus, a sedimentary source for carbon is not supported by field
557 observations. Accordingly, we infer that CO₂ was externally introduced in the lower crust,
558 very likely from a mantle source. This is in agreement with previous studies that suggested
559 the mantle as a common source for CO₂ in high temperature granulites (e.g. Hoefs & Touret,
560 1975; Jackson, Matthey, & Harris, 1988; Santosh & Omori, 2008; Touret & Huizenga, 2011).

561 However, we also emphasize that without a rigorous isotopic determination for carbon, the
562 origin of CO₂ remains uncertain. On the other hand, the minor N₂ amount detected in Type C
563 granulites is interpreted to derive from the breakdown of NH₄⁺-bearing micas during anatexis
564 (e.g. Moin, Guillot, & Gibert, 1994; Cesare et al., 2007).

565 For the Gruf Complex, if an external source for CO₂ is assumed, the different CO₂
566 concentrations in the MI may be related to small-scale heterogeneities of the fluid
567 composition within the matrix surrounding the growing peritectic garnets.

568

569 **5.3 Rheology of anatectic melt**

570 Granulites from the Gruf Complex represent UHT residues of metapelitic lower crustal rocks
571 which lost *c.* 40-50% of melt during anatexis (Galli et al., 2011). Partial melting generated
572 rhyolitic melts that are now preserved as MI within peritectic garnets in the granulites. The
573 investigation of these MI not only allows to retrieve the chemical composition of anatectic
574 melts but also to calculate melt density and viscosity, two crucial physical properties to
575 understand melt rheology and its mobilization through the crust. Assuming a pressure of 9
576 kbar and a temperature of 875°C, which corresponds to the experimental re-homogenization
577 temperature, an average melt density of 2.33 g/cm³ was determined using the program
578 DensityX by Iacovino and Till (2019). On the other hand, melt viscosities calculated at
579 875°C range between 10^{3.9}-10^{4.5} Pa·s, applying the equation of Scaillet, Holtz, Pichavant, &
580 Schmidt (1996) and between 10^{4.1}-10^{4.8} Pa·s, using the equation of Giordano, Russell, &
581 Dingwell (2008). These values are ~2 orders of magnitude lower than viscosities estimated
582 for nearly anhydrous crustal melts at 900°C (e.g. Hess and Dingwell, 1996) but are consistent
583 within error with the experimental values obtained by Ardia, Giordano, and Schmidt (2008)
584 for rhyolitic melts between 5 and 15 kbar at similar water contents (see Figure S4).
585 Moreover, viscosities for MI from the Gruf Complex overlap the range of viscosities obtained
586 by Bartoli et al. (2013) for melts in metasedimentary metatexites at the contact with the
587 Ronda peridotite, in the Spanish Betic Cordillera.
588 The determination of viscosity and density allows us then to speculate on the ascent velocity
589 of the melt from its source. In our calculations, melt ascent is approximated as simple porous

590 flow following Turcotte & Schubert (2002). We assume an average melt viscosity of $10^{4.4 \pm 0.3}$
591 Pa·s and an average melt density of 2.33 g/cm^3 as calculated from MI, an average density of
592 3.10 g/cm^3 for the lower crust (Hacker, Kelemen, & Behn, 2015) and a grain size for the
593 matrix of 1-2 mm. For porosities of 8% and 25%, which respectively correspond to the liquid
594 percolation threshold (LPT) and the melt escape threshold (MET) of Vigneresse, Barbey, &
595 Cuney (1996), melt velocities range between 5 and 250 mm/year (see Table S6).

596 It has to be stressed that these melt velocities are calculated for a constant temperature of $T =$
597 875°C and are relative to a static, homogeneous solid matrix. Therefore, our calculations give
598 only a first-order approximation on the ascending behaviour of pristine anatectic melts at the
599 onset of crustal anatexis approaching ultra-high temperatures. In fact, melting in the lower
600 crust occurs in a dynamic, heterogeneous environment, where several factors may affect melt
601 ascent. Ascent velocities of magmas may be strongly increased by deviatoric stresses
602 (Sawyer 1994) or by the occurrence of high permeability anomalies in the crust, such as large
603 scale shear zones, which may be able to provide preferred pathways for the ascending melt
604 due to their high anisotropy. Furthermore, at high melt fractions it is expected that the
605 pervasively distributed melt might be channelized by porosity waves (e.g. Connolly &
606 Podladchikov, 2015), resulting in an enhanced melt migration rate. On the other hand, syn-
607 anatexis exhumation of partly molten crustal portions to upper and colder crustal levels
608 would decrease the temperature and therefore lower the melt velocity and its ability to be
609 extracted. Cooling induces a strong increase of melt viscosity but only a limited density
610 decrease, which is reflected in a dramatic drop of the melt velocity (see Table S6). Since
611 exhumation favours high cooling rates, high exhumation rates in a dynamic crust will have a
612 negative feedback on the melt velocity. Hence, at high cooling rates melt extraction would
613 become less efficient and (at least) part of the produced UHT melt would be likely stuck and
614 move coupled with the ascending hot crust (Teyssier & Whitney, 2002). Such scenario is

615 expected to become more common at anatectic temperature $<800^{\circ}\text{C}$ because melt velocities
616 at 800°C are almost one order of magnitude lower than at 900°C (see Table S6).

617

618 **6. CONCLUSIONS**

619 Evidence that the Earth's continental crust has the ability to attain, on a regional scale, ultra-
620 high temperatures has been widely reported. Under these conditions, middle and lower crust
621 undergo substantial modifications that have important consequences on their rheological
622 properties, which, in turn, may largely affect the mass transfer at the crust-mantle boundary.
623 Peraluminous, K-rich rhyolitic melt inclusions observed in garnet porphyroblasts of UHT
624 granulites from the Gruf Complex are the result of crustal anatexis, the latter driven by the
625 breakdown of biotite. The presence of primary melt and fluid inclusions with both a COH
626 volatile component suggests that anatexis initially started due to dehydration melting
627 reactions and was promoted by the influx of an external $\text{CO}_2+\text{H}_2\text{O}$ fluid. Although the source
628 of CO_2 cannot be undoubtedly ascertained, we infer that a mantle origin for the carbon is a
629 more likely explanation. On the other hand, the high H_2O content measured in the melt
630 inclusions suggests that anatectic melts up to UHT conditions are less dry than commonly
631 assumed, with relevant implications for the viscosity of anatectic melts. The production of
632 low density rhyolitic melts in the lower crust may induce large-scale weakening (Rosenberg
633 and Handy, 2005) that ultimately may lead to the lateral flow of mountain belts (Jamieson et
634 al. 2011) or to the formation of domes and crustal diapirs (e.g. Gerya, Perchuk, Maresch, &
635 Willner, 2004; Teyssier & Whitney, 2002). The latter mechanism can be an effective
636 geological process that may trigger the exhumation of high-grade metamorphic rocks.
637 Moreover, the potassic to ultrapotassic composition of the analysed anatectic melts may
638 indicate that crustal anatexis can have a larger impact in the redistribution of heat-producing
639 elements (such as K_2O), with important implications for the thermal structure of the

640 continental crust (e.g. Antonelli, DePaolo, Chacko, Grew, & Rubatto 2019; Hacker et al.
641 2015).

642 This study shows that anatectic melt inclusions provide a fundamental insight into the
643 comprehension of the melting regime in UHT terranes and the chemical differentiation of the
644 lower crust.

645

646 **ACKNOWLEDGEMENTS**

647

648 We thank Leonardo Tauro for the preparation of high quality polished thin sections, Raul
649 Carampin (University of Padova) and Andrea Risplendente (University di Milano) for their
650 help during electron microprobe analyses. O.G. thanks D. Grassi for stimulating and fruitful
651 discussions. We thank C. Wei and an anonymous reviewer for their constructive reviews and
652 J. Baldwin for editorial handling.

653 This research was supported by the Italian Ministry of Education, University, Research
654 (Grant SIR RBSI14Y7PF to O.B. and Grant PRIN 2017ZE49E7 to B.C.), the University of
655 Padova (research grant BART_SID19_01 to O.B.) and the CARIPARO (Cassa di Risparmio
656 di Padova e Rovigo) project MAKEARTH (to F.F.). The German Federal Ministry for
657 Education and Research and the Deutsche Forschungsgemeinschaft (Project FE 1527/2-1 and
658 FE 1527/2-2 to S.F.) are gratefully acknowledged for funding the present research work. The
659 NanoSIMS facility at the Muséum National d'Histoire Naturelle in Paris was established by
660 funds from the CNRS, Région Ile de France, Ministère délégué à l'Enseignement supérieur et
661 à la Recherche, and the Muséum National d'Histoire Naturelle.

662

663

664

665 **REFERENCES**

666

667 Acosta-Vigil, A., London, D., Morgan, G. B., & Dewers, T. A. (2003). Solubility of excess
668 alumina in hydrous granitic melts in equilibrium with peraluminous minerals at 700-
669 800 °C and 200 MPa, and applications of the aluminum saturation index.

670 *Contributions to Mineralogy and Petrology*, 146, 100-119.

671 <https://doi.org/10.1007/s00410-003-0486-6>

672 Acosta-Vigil, A., Cesare, B., London, D., & Morgan, G.B. (2007). Microstructures and
673 composition of melt inclusions in a crustal anatectic environment, represented by
674 metapelitic enclaves within El Hoyazo dacites, SE Spain. *Chemical Geology*, 237,
675 450-465. <https://doi.org/10.1016/j.chemgeo.2006.07.014>

676 Acosta-Vigil, A., Barich, A., Bartoli, O., Garrido, C.J., Cesare, B., Remusat, L., Poli, S.,
677 & Raepsaet, C. (2016). The composition of nanogranitoids in migmatites overlying
678 the Ronda peridotites (Betic Cordillera, S Spain): the anatectic history of a
679 polymetamorphic basement. *Contributions to Mineralogy and Petrology*, 171, 1-31.
680 <https://doi.org/10.1007/s00410-016-1230-3>

681 Acosta-Vigil, A., London, D., VI, G. B. M., Cesare, B., Buick, I., Hermann, J., & Bartoli, O.
682 (2017). Primary crustal melt compositions: Insights into the controls, mechanisms and
683 timing of generation from kinetics experiments and melt inclusions. *Lithos*, 286, 454-
684 479. <http://dx.doi.org/10.1016/j.lithos.2017.05.020>

685 Antonelli, M. A., De Paolo, D. J., Chacko, T., Grew, E. S., & Rubatto, D. (2019). Radiogenic
686 Ca isotopes confirm post-formation K depletion of lower crust. *Geochemical
687 perspectives letters*, 9, 43-48. doi: 10.7185/geochemlet.1904

688 Ardia, P., Giordano, D., & Schmidt, M. W. (2008). A model for the viscosity of rhyolite as a
689 function of H₂O-content and pressure: A calibration based on centrifuge piston

- 690 cylinder experiments. *Geochimica et Cosmochimica Acta*, 72, 6103-6123.
691 <https://doi.org/10.1016/j.gca.2008.08.025>
- 692 Aubaud, C., Withers, A. C., Hirschmann, M. M., Guan, Y., Leshin, L. A., Mackwell, S. J., &
693 Bell, D. R. (2007). Intercalibration of FTIR and SIMS for hydrogen measurements in
694 glasses and nominally anhydrous minerals. *American Mineralogist*, 92, 811–828.
695 <https://doi.org/10.2138/am.2007.2248>
- 696 Bartoli, O., Cesare, B., Poli, S., Bodnar, R.J., Acosta-Vigil, A., Frezzotti, M.L., & Meli, S.
697 (2013). Recovering the composition of melt and the fluid regime at the onset of
698 crustal anatexis and S-type granite formation. *Geology*, 41, 115-118.
699 <https://doi.org/10.1130/G33455.1>
- 700 Bartoli, O., Cesare, B., Remusat, L., Acosta-Vigil, A., & Poli, S. (2014). The H₂O content of
701 granite embryos. *Earth and Planetary Science Letters*, 395, 281–290.
702 <https://doi.org/10.1016/j.epsl.2014.03.031>
- 703 Bartoli, O., Acosta-Vigil, A., & Cesare, B. (2015). High-temperature metamorphism and
704 crustal melting: working with melt inclusions. *Periodico di Mineralogia*, 84, 591-614.
705 <http://dx.doi.org/10.2451/2015PM0434>
- 706 Bartoli, O., Acosta-Vigil, A., Tajčmanová, L., Cesare, B., & Bodnar, R.J. (2016). Using
707 nanogranitoids and phase equilibria modeling to unravel anatexis in the crustal
708 footwall of the Ronda peridotites (Betic Cordillera, S Spain), *Lithos*, 256-257, 282-
709 299. <https://doi.org/10.1016/j.lithos.2016.03.016>
- 710 Bartoli, O., Acosta-Vigil, A., Cesare, B., Remusat, L., Gonzalez-Cano, A., Wälle, M.,
711 Tajčmanová, L., & Langone, A. (2019). Geochemistry of Eocene-Early Oligocene
712 low-temperature crustal melts from Greater Himalayan Sequence (Nepal): a
713 nanogranitoid perspective. *Contributions to Mineralogy and Petrology*, 174, 82.
714 <https://doi.org/10.1007/s00410-019-1622-2>

- 715 Behrens, H., & Jantos, N. (2001). The effect of anhydrous composition on water solubility in
716 granitic melts. *American Mineralogist*, *86*, 14-20. [https://doi.org/10.2138/am-2001-](https://doi.org/10.2138/am-2001-0102)
717 0102
- 718 Boulard, E., Guyot, F., & Fiquet, G. (2012). The influence on Fe content on Raman spectra
719 and unit cell parameters of magnesite-siderite solid solutions. *Physics and Chemistry*
720 *of Minerals*, *39*, 239-246. <https://doi.org/10.1007/s00269-011-0479-3>
- 721 Brandt, S., Will, T.M., & Klemd, R. (2007). Magmatic loading in the proterozoic Epupa
722 Complex, NW Namibia, as evidenced by ultrahigh-temperature sapphirine-bearing
723 orthopyroxene-sillimanite-quartz granulites. *Precambrian Research*, *153*, 143-178.
724 <https://doi.org/10.1016/j.precamres.2006.11.016>
- 725 Brooker, R.A., Kohn, S.C., Holloway, J.R., McMillan, P.F., & Carroll, M.R. (1999).
726 Solubility, speciation and dissolution mechanisms for CO₂ in melts on the NaAlO₂-
727 SiO₂ join. *Geochimica et Cosmochimica Acta*, *63*, 3549-3565.
728 [https://doi.org/10.1016/S0016-7037\(99\)00196-9](https://doi.org/10.1016/S0016-7037(99)00196-9)
- 729 Brown, M., Korhonen, F.J., & Siddoway, C.S. (2011). Organizing melt flow through the
730 crust. *Elements*, *7*, 261-266. <https://doi.org/10.2113/gselements.7.4.261>
- 731 Brown, M., & Johnson, T. (2018). Secular change in metamorphism and the onset of global
732 plate tectonics. *American Mineralogist*, *103*, 181-196. [https://doi.org/10.2138/am-](https://doi.org/10.2138/am-2018-6166)
733 2018-6166
- 734 Bucher-Nurminen, K., & Droop, G. (1983). The metamorphic evolution of garnet-cordierite-
735 sillimanite-gneisses of the Gruf-Complex, Eastern Pennine Alps. *Contributions to*
736 *Mineralogy and Petrology*, *84*, 215-227. <https://doi.org/10.1007/BF00371287>
- 737 Bureau, H., Trocellier, P., Shaw, C., Khodja, H., Bolfan-Casanova, N., & Demouchy, S.
738 (2003). Determination of the concentration of water dissolved in glasses and minerals
739 using nuclear microprobe. *Nuclear Instruments & Methods in Physics Research*,

- 740 *Section B: Beam Interactions with Materials and Atoms*, 210, 449–454.
 741 [https://doi.org/10.1016/S0168-583X\(03\)01074-7](https://doi.org/10.1016/S0168-583X(03)01074-7)
- 742 Carvalho, B. B., Sawyer, E. W., & Janasi, V. A. (2016). Crustal reworking in a shear zone:
 743 Transformation of metagranite to migmatite. *Journal of Metamorphic Geology*, 34,
 744 237–264. <https://doi.org/10.1111/jmg.12180>
- 745 Carvalho, B.B., Bartoli, O., Ferri, F., Cesare, B., Ferrero, S., Remusat, L., Capizzi, L.S. &
 746 Poli, S. (2019). Anatexis and fluid regime of the deep continental crust: New clues
 747 from melt and fluid inclusions in metapelitic migmatites from Ivrea Zone (NW Italy).
 748 *Journal of Metamorphic Geology*, 37, 951-975. <https://doi.org/10.1111/jmg.12463>
- 749 Carvalho, B. B., Bartoli, O., Cesare, B., Tacchetto, T., Gianola, O., Ferri, F., Aradi, L.E., &
 750 Szabó, C. (2020). Primary CO₂-bearing fluid inclusions in granulitic garnet usually do
 751 not survive. *Earth and Planetary Science Letters*, 536, 116170.
 752 <https://doi.org/10.1016/j.epsl.2020.116170>
- 753 Castro, N. A., de Araujo, C. E. G., Basei, M. A., Osako, L. S., Nutman, A. A., & Liu, D.
 754 (2012). Ordovician A-type granitoid magmatism on the Ceará Central Domain,
 755 Borborema Province, NE-Brazil. *Journal of South American Earth Sciences*, 36, 18-
 756 31. <https://doi.org/10.1016/j.jsames.2011.11.007>
- 757 Cesare, B., Marchesi, C., Hermann, J., & Gómez-Pugnaire, M.T. (2003). Primary melt
 758 inclusions in andalusite from anatectic graphitic metapelites: implications for the
 759 position of the Al₂SiO₅ triple point. *Geology*, 31, 573-576.
 760 [https://doi.org/10.1130/0091-7613\(2003\)031<0573:PMIIAF>2.0.CO;2](https://doi.org/10.1130/0091-7613(2003)031<0573:PMIIAF>2.0.CO;2)
- 761 Cesare, B., Maineri, C., Baron Toaldo, A., Pedron, D., & Acosta-Vigil, A. (2007).
 762 Immiscibility between carbonic fluids and granitic melts during crustal anatexis: a
 763 fluid and melt inclusion study in the enclaves of the Neogene Volcanic Province of SE

- 764 Spain. *Chemical Geology*, 237, 433-449.
765 <https://doi.org/10.1016/j.chemgeo.2006.07.013>
- 766 Cesare, B., Ferrero, S., Salvioli-Mariani, E., Pedron, D., & Cavallo, A. (2009). “Nanogranite”
767 and glassy inclusions: The anatectic melt in migmatites and granulites. *Geology*, 37,
768 627-630. <https://doi.org/10.1130/G25759A.1>
- 769 Cesare, B., Acosta-Vigil, A., Bartoli, O., & Ferrero, S., (2015). What can we learn from melt
770 inclusions in migmatites and granulites? *Lithos*, 239, 186-216.
771 <https://doi.org/10.1016/j.lithos.2015.09.028>
- 772 Chappell, B. W., & White, A. J. R. (1992). I-and S-type granites in the Lachlan Fold Belt.
773 *Earth and Environmental Science Transactions of the Royal Society of Edinburgh*, 83,
774 1-26. <https://doi.org/10.1017/S0263593300007720>
- 775 Clemens, J.D., Holloway, J.R., & White, A.J.R. (1986). Origin of an A-type granite:
776 experimental constraints. *American Mineralogist*, 71, 317-324.
- 777 Clemens, J.D., & Stevens, G. (2016). Melt segregation and magma interactions during crustal
778 melting: breaking out of the matrix. *Earth-Science Reviews*, 160, 333-349.
779 <https://doi.org/10.1016/j.earscirev.2016.07.012>
- 780 Connolly, J. A., & Podladchikov, Y. Y. (2015). An analytical solution for solitary porosity
781 waves: dynamic permeability and fluidization of nonlinear viscous and viscoplastic
782 rock. *Geofluids*, 15, 269-292. <https://doi.org/10.1111/gfl.12110>
- 783 Créon, L., Levresse, G., Remusat, L., Bureau, H., & Carrasco-Núñez, G. (2018). New method
784 for initial composition determination of crystallized silicate melt inclusions. *Chemical*
785 *Geology*, 483, 162–173. <https://doi.org/10.1016/j.chemgeo.2018.02.038>
- 786 de Almeida, C. N., de Pinho Guimarães, I., & da Silva Filho, A. F. (2002). A-type post-
787 collisional granites in the Borborema province-NE Brazil: The Queimadas pluton.
788 *Gondwana Research*, 5, 667-681. [https://doi.org/10.1016/S1342-937X\(05\)70637-7](https://doi.org/10.1016/S1342-937X(05)70637-7)

- 789 Droop, G. T. R., Clemens, J. D., & Dalrymple, D. J. (2003). Processes and conditions during
790 contact anatexis, melt escape and restite formation: the Huntly Gabbro Complex, NE
791 Scotland. *Journal of Petrology*, *44*, 995-1029.
792 <https://doi.org/10.1093/petrology/44.6.995>
- 793 Dubessy, J., Poty, B., & Ramboz, C. (1989). Advances in C-O-H-N-S fluid geochemistry
794 based on micro-Raman spectrometric analysis of fluid inclusions. *European Journal*
795 *of Mineralogy*, *1*, 517-534.
- 796 Esposito, R., Lamadrid, H. M., Redi, D., Steele-MacInnis, M., Bodnar, R. J., Manning, C. E.,
797 De Vivo, B., Cannatelli, C., & Lima, A. (2016). Detection of liquid H₂O in vapor
798 bubbles in reheated melt inclusions: Implications for magmatic fluid composition and
799 volatile budgets of magmas? *American Mineralogist*, *101*, 1691-1695.
800 <https://doi.org/10.2138/am-2016-5689>
- 801 Ferrero, S., Bartoli, O., Cesare, B., Salvioli-Mariani, E., Acosta-Vigil, A., Cavallo, A.,
802 Groppo, C., & Battiston, S. (2012). Microstructures of melt inclusions in anatectic
803 metasedimentary rocks. *Journal of Metamorphic Geology*, *30*, 303-322.
804 <https://doi.org/10.1111/j.1525-1314.2011.00968.x>
- 805 Ferrero, S., Braga, R., Berkesi, M., Cesare, B., & Laridhi Ouazaa, N. (2014). Production of
806 metaluminous melt during fluid-present anatexis: an example from the Maghrebian
807 basement, La Galite Archipelago, central Mediterranean. *Journal of Metamorphic*
808 *Geology*, *32*, 209-225. <https://doi.org/10.1111/jmg.12068>
- 809 Ferrero, S., Wunder, B., Walczak, K., O'Brien, P.J., & Ziemann, M.A. (2015). Preserved near
810 ultrahigh-pressure melt from continental crust subducted to mantle depths.
811 *Geology*, *43*, 447-450. <https://doi.org/10.1130/G36534.1>
- 812 Ferrero, S., Wunder, B., Ziemann, M. A., Wälle, M., & O'Brien, P. J. (2016). Carbonatitic
813 and granitic melts produced under conditions of primary immiscibility during anatexis

- 814 in the lower crust. *Earth and Planetary Science Letters*, 454, 121-131.
815 <https://doi.org/10.1016/j.epsl.2016.08.043>
- 816 Ferrero, S., O'Brien, P. J., Borghini, A., Wunder, B., Wälle, M., Günter, C., & Ziemann, M.
817 A. (2019). A treasure chest full of nanogranitoids: an archive to investigate crustal
818 melting in the Bohemian Massif. *Geological Society, London, Special Publications*,
819 478, 13-38. <https://doi.org/10.1144/SP478.19>
- 820 Florisbal, L. M., de Fátima Bitencourt, M., Nardi, L. V. S., & Conceição, R. V. (2009). Early
821 post-collisional granitic and coeval mafic magmatism of medium-to high-K tholeiitic
822 affinity within the Neoproterozoic Southern Brazilian Shear Belt. *Precambrian*
823 *Research*, 175, 135-148. <https://doi.org/10.1016/j.precamres.2009.09.003>
- 824 Galli A., Le Bayon B., Schmidt M.W., Burg J.-P., Caddick M.J., & Reusser E. (2011).
825 Granulites and charnockites of the Gruf Complex: Evidence for Permian ultra-high
826 temperature metamorphism in the Central Alps. *Lithos*, 124, 17-45.
827 <https://doi.org/10.1016/j.lithos.2010.08.003>
- 828 Galli, A., Le Bayon, B., Schmidt, M.W., Burg, J.-P., Reusser, E., Sergeev, S.A., & Larionov,
829 A. (2012). U-Pb zircon dating of the Gruf Complex: disclosing the late Variscan
830 granulitic lower crust of Europe stranded in the Central Alps. *Contributions to*
831 *Mineralogy and Petrology*, 163, 353-378. <https://doi.org/10.1007/s00410-011-0676-6>
- 832 Galli, A., Le Bayon, B., Schmidt, M. W., Burg, J. P., & Reusser, E. (2013).
833 Tectonometamorphic history of the Gruf complex (Central Alps): exhumation of a
834 granulite–migmatite complex with the Bergell pluton. *Swiss Journal of Geosciences*,
835 106, 33-62. <https://doi.org/10.1007/s00015-013-0120-1>
- 836 Gerya, T. V., Perchuk, L. L., Maresch, W. V., & Willner, A. P. (2004). Inherent gravitational
837 instability of hot continental crust: Implications for doming and diapirism in granulite

- 838 facies terrains. *Special paper - Geological Society of America*, 380, 97-116.
- 839 <https://doi.org/10.1130/0-8137-2380-9.97>
- 840 Ghani, A. A., Hazad, F. I., Jamil, A., Xiang, Q. L., Ismail, W. N. A. W., Chung, S. L., ... &
841 Mohd, M.R. (2014). Permian ultrafelsic A-type granite from Besar Islands group,
842 Johor, peninsular Malaysia. *Journal of Earth System Science*, 123, 1857-1878.
843 <https://doi.org/10.1007/s12040-014-0501-5>
- 844 Gianola, O., Schmidt, M.W., von Quadt, A., Peytcheva, I., Luraschi, P., & Reusser, E.
845 (2014). Continuity in geochemistry and time of the Tertiary Bergell intrusion (Central
846 Alps). *Swiss Journal of Geosciences*, 107, 197-222. [https://doi.org/10.1007/s00015-](https://doi.org/10.1007/s00015-014-0174-8)
847 [014-0174-8](https://doi.org/10.1007/s00015-014-0174-8)
- 848 Giordano, D., Russell, J. K., & Dingwell, D. B. (2008). Viscosity of magmatic liquids: a
849 model. *Earth and Planetary Science Letters*, 271, 123-134.
850 <https://doi.org/10.1016/j.epsl.2008.03.038>
- 851 Goodenough, K. M., Upton, B. G. J., & Ellam, R. M. (2000). Geochemical evolution of the
852 Ivigtut granite, South Greenland: a fluorine-rich “A-type” intrusion. *Lithos*, 51, 205-
853 221. [https://doi.org/10.1016/S0024-4937\(99\)00064-X](https://doi.org/10.1016/S0024-4937(99)00064-X)
- 854 Grant, J.A. (2009). THERMOCALC and experimental modelling of melting of pelite, Morton
855 Pass, Wyoming. *Journal of metamorphic geology*, 27, 571-578.
856 <https://doi.org/10.1111/j.1525-1314.2009.00846.x>
- 857 Guevara, V. E., & Caddick, M. J. (2016). Shooting at a moving target: Phase equilibria
858 modelling of high-temperature metamorphism. *Journal of Metamorphic Geology*, 34,
859 209-235. <https://doi.org/10.1111/jmg.12179>
- 860 Hacker, B. R., Kelemen, P. B., & Behn, M. D. (2015). Continental lower crust. *Annual*
861 *Review of Earth and Planetary Sciences*, 43, 167-205.
862 <https://doi.org/10.1146/annurev-earth-050212-124117>

- 863 Harley, S.L., Hensen, B.J., & Sheraton, J.W. (1990). Two-stage decompression in
864 orthopyroxene–sillimanite granulites from Forefinger Point, Enderby Land,
865 Antarctica: implications for the evolution of the Archean Napier Complex. *Journal of*
866 *metamorphic geology*, 8, 591-613. [https://doi.org/10.1111/j.1525-](https://doi.org/10.1111/j.1525-1314.1990.tb00490.x)
867 [1314.1990.tb00490.x](https://doi.org/10.1111/j.1525-1314.1990.tb00490.x)
- 868 Harley, S. L. (1998). On the occurrence and characterization of ultrahigh-temperature crustal
869 metamorphism. In: Treloar, P.J., O'Brian, P.J. (Eds.), What drives metamorphism and
870 metamorphic reactions? *Geological Society, London, Special Publications*, 138, 81-
871 107. <https://doi.org/10.1144/GSL.SP.1996.138.01.06>
- 872 Harley, S.L. (2008). Refining the P-T records of UHT crustal metamorphism. *Journal of*
873 *metamorphic geology*, 26, 125-154. [https://doi.org/10.1111/j.1525-](https://doi.org/10.1111/j.1525-1314.2008.00765.x)
874 [1314.2008.00765.x](https://doi.org/10.1111/j.1525-1314.2008.00765.x)
- 875 Hess, K. U., & Dingwell, D. B. (1996). Viscosities of hydrous leucogranitic melts: A non-
876 Arrhenian model. *American Mineralogist*, 81, 1297-1300.
- 877 Hoefs, J., & Touret, J. (1975). Fluid inclusion and carbon isotope study from Bamble
878 granulites (South Norway). *Contributions to Mineralogy and Petrology*, 52, 165-174.
879 <https://doi.org/10.1007/BF00457292>
- 880 Holland, T., & Powell, R. (2001). Calculation of phase relations involving haplogranitic
881 melts using an internally consistent thermodynamic dataset. *Journal of Petrology*, 42,
882 673-683. <https://doi.org/10.1093/petrology/42.4.673>
- 883 Holness, M. B., & Sawyer, E. W. (2008). On the pseudomorphing of melt-filled pores during
884 the crystallization of migmatites. *Journal of Petrology*, 49, 1343-1363.
885 <https://doi.org/10.1093/petrology/egn028>

- 886 Holtz, F., Johannes, W., Tamic, N., & Behrens, H. (2001). Maximum and minimum water
887 contents of granitic melts generated in the crust: a reevaluation and implications.
888 *Lithos*, 56, 1-14. [https://doi.org/10.1016/S0024-4937\(00\)00056-6](https://doi.org/10.1016/S0024-4937(00)00056-6)
- 889 Iacovino, K., & Till, C. B. (2019). DensityX: A program for calculating the densities of
890 magmatic liquids up to 1,627° C and 30 kbar. *Volcanica*, 2, 1-10.
891 <https://doi.org/10.30909/vol.02.01.0110>
- 892 Jackson, D. H., Matthey, D. P., & Harris, N. B. W. (1988). Carbon isotope compositions of
893 fluid inclusions in charnockites from southern India. *Nature*, 333, 167.
894 <https://doi.org/10.1038/333167a0>
- 895 Jamieson, R.A., Unsworth, M.J., Harris, N.B.W., Rosenberg, C.L., & Schulmann, K. (2011).
896 Crustal melting and the flow of mountains. *Elements*, 7, 253-260.
897 <https://doi.org/10.2113/gselements.7.4.253>
- 898 Jung, S., Hoernes, S., & Mezger, K. (2000). Geochronology and petrogenesis of Pan-African,
899 syn-tectonic, S-type and post-tectonic A-type granite (Namibia): products of melting
900 of crustal sources, fractional crystallization and wall rock entrainment. *Lithos*, 50,
901 259-287. [https://doi.org/10.1016/S0024-4937\(99\)00059-6](https://doi.org/10.1016/S0024-4937(99)00059-6)
- 902 Kalsbeek, F., Jepsen, H. F., & Jones, K. A. (2001). Geochemistry and petrogenesis of S-type
903 granites in the East Greenland Caledonides. *Lithos*, 57, 91-109.
904 [https://doi.org/10.1016/S0024-4937\(01\)00038-X](https://doi.org/10.1016/S0024-4937(01)00038-X)
- 905 Kelsey, D.E. (2008). On ultrahigh-temperature crustal metamorphism. *Gondwana Research*,
906 13, 1-29. <https://doi.org/10.1016/j.gr.2007.06.001>
- 907 Kelsey, D.E., & Hand, M. (2015). On ultrahigh temperature crustal metamorphism: phase
908 equilibria, trace element thermometry, bulk composition, heat sources, timescales and
909 tectonic settings. *Geoscience Frontiers*, 6, 311-356.
910 <https://doi.org/10.1016/j.gsf.2014.09.006>

- 911 King, P. L., White, A. J. R., Chappell, B. W., & Allen, C. M. (1997). Characterization and
912 origin of aluminous A-type granites from the Lachlan Fold Belt, southeastern
913 Australia. *Journal of Petrology*, 38, 371-391. <https://doi.org/10.1093/etroj/38.3.371>
- 914 King, P. L., Chappell, B. W., Allen, C. M., & White, A. J. R. (2001). Are A-type granites the
915 high-temperature felsic granites? Evidence from fractionated granites of the Wangrah
916 Suite. *Australian Journal of Earth Sciences*, 48, 501-514.
917 <https://doi.org/10.1046/j.1440-0952.2001.00881.x>
- 918 Lamadrid, H. M., Lamb, W. M., Santosh, M., & Bodnar, R. J. (2014). Raman spectroscopic
919 characterization of H₂O in CO₂-rich fluid inclusions in granulite facies metamorphic
920 rocks. *Gondwana Research*, 26, 301-310. <https://doi.org/10.1016/j.gr.2013.07.003>
- 921 Le Breton, N., & Thompson, A.B. (1988). Fluid-absent (dehydration) melting of biotite in
922 metapelites in the early stages of crustal anatexis. *Contributions to Mineralogy and
923 Petrology*, 99, 226-237. <https://doi.org/10.1007/BF00371463>
- 924 Liati, A., Gebauer, D., & Fanning, M. (2000). U-Pb SHRIMP dating of zircon from the
925 Novate granite (Bergell, Central Alps): evidence for Oligocene-Miocene magmatism,
926 Jurassic/Cretaceous continental rifting and opening of the Valais trough.
927 *Schweizerische Mineralogische und Petrographische Mitteilungen*, 80, 305-316.
928 <http://dx.doi.org/10.5169/seals-60970>
- 929 Lowenstern, J. B. (1995). Applications of silicate-melt inclusions to the study of magmatic
930 volatiles. *Magmas, Fluids, and Ore Deposits*, 23, 71-99.
- 931 Marchildon, N., & Brown M. (2001). Melt segregation in late syn-tectonic anatectic
932 migmatites: an example from the Onawa contact aureole, Maine, USA. *Physics and
933 Chemistry of the Earth, Part A: Solid Earth and Geodesy*, 26, 225-229.
934 [https://doi.org/10.1016/S1464-1895\(01\)00049-7](https://doi.org/10.1016/S1464-1895(01)00049-7)

- 935 McDermott, F., Harris, N. B. W., & Hawkesworth, C. J. (2000). Geochemical constraints on
936 the petrogenesis of Pan-African A-type granites in the Damara Belt, Namibia. *Henno*
937 *Martin Commemorative Volume: Communications of the Geological Survey of*
938 *Namibia, Special Publication of the Geol. Survey of Namibia, 12*, 139-148.
- 939 Milord, I., Sawyer, E. W., & Brown, M. (2001). Formation of diatexite migmatite and granite
940 magma during anatexis of semi-pelitic metasedimentary rocks: an example from St.
941 Malo, France. *Journal of Petrology, 42*, 487-505.
942 <https://doi.org/10.1093/petrology/42.3.487>
- 943 Moin, B., Guillot, C., & Gibert, F. (1994). Controls of the composition of nitrogen-rich fluids
944 originating from reaction with graphite and ammonium-bearing biotite. *Geochimica et*
945 *Cosmochimica Acta, 58*, 5503-5523. [https://doi.org/10.1016/0016-7037\(94\)90246-1](https://doi.org/10.1016/0016-7037(94)90246-1)
- 946 Montel, J-M., & Vielzeuf, D. (1997). Partial melting of metagreywackes, part II.
947 Compositions of minerals and melts. *Contributions to Mineralogy and Petrology,*
948 *128*, 176-196. <https://doi.org/10.1007/s004100050302>
- 949 Morgan, G. B., & London, D. (2005). Effect of current density on the electron microprobe
950 analysis of alkali aluminosilicate glasses. *American Mineralogist, 90*, 1131-1138.
951 <https://doi.org/10.2138/am.2005.1769>
- 952 Mouri, H., Guiraud, M., & Hensen, B. J. (1996). Petrology of phlogopite-sapphirine-bearing
953 Al-Mg granulites from Ihouhaouene, In Ouzzal, Hoggar, Algeria: an example of
954 phlogopite stability at high temperature. *Journal of metamorphic Geology, 14*, 725-
955 738. <https://doi.org/10.1111/j.1525-1314.1996.00045.x>
- 956 Nagel, T., De Capitani, C., & Frey, M. (2002). Isograds and P-T evolution in the eastern
957 Lepontine Alps (Graubünden, Switzerland). *Journal of Metamorphic Geology, 20*,
958 309-324. <https://doi.org/10.1046/j.1525-1314.2002.00368.x>

- 959 Nandakumar, V., & Harley, S. L. (2000). A reappraisal of the pressure-temperature path of
960 granulites from the Kerala Khondalite Belt, southern India. *The Journal of Geology*,
961 *108*, 687-703. <https://doi.org/10.1086/317947>
- 962 Ni, H., & Keppler, H. (2013). Carbon in silicate melts. *Reviews in Mineralogy &*
963 *Geochemistry*, *75*, 251-287. <https://doi.org/10.2138/rmg.2013.75.9>
- 964 Oalman, J., Duesterhoeft, E., Möller, A., & Bousquet, R. (2019). Constraining the pressure–
965 temperature evolution and geodynamic setting of UHT granulites and migmatitic
966 paragneisses of the Gruf Complex, Central Alps. *International Journal of Earth*
967 *Sciences*, *108*, 911-930. <https://doi.org/10.1007/s00531-019-01686-x>
- 968 Oberli, F., Meier, M., Berger, A., Rosenberg, C.L., & Gieré, R. (2004). U-Th-Pb and
969 $^{230}\text{Th}/^{238}\text{U}$ disequilibrium isotope systematics: Precise accessory mineral chronology
970 and melt evolution tracing in the Alpine Bergell intrusion. *Geochimica et*
971 *Cosmochimica Acta*, *68*, 2543-2560. <https://doi.org/10.1016/j.gca.2003.10.017>
- 972 Patiño Douce, A. E., & Johnston, A. D. (1991). Phase equilibria and melt productivity in the
973 pelitic system: implications for the origin of peraluminous granitoids and aluminous
974 granulites. *Contributions to Mineralogy and Petrology*, *107*, 202-218.
975 <https://doi.org/10.1007/BF00310707>
- 976 Rosenberg, C. L., & Handy, M. R. (2005). Experimental deformation of partially melted
977 granite revisited: implications for the continental crust. *Journal of metamorphic*
978 *Geology*, *23*, 19-28. <https://doi.org/10.1111/j.1525-1314.2005.00555.x>
- 979 Rudnick, R.L. (1995). Making continental crust. *Nature*, *378*, 571-578.
980 <https://doi.org/10.1038/378571a0>
- 981 Samperton, K.M., Schoene, B., Cottle, J.M., Keller, C.B., Crowley, J.L., & Schmitz, M.D.
982 (2015). Magma emplacement, differentiation and cooling in the middle crust:
983 integrated zircon geochronological-geochemical constraints from the Bergell

- 984 intrusion, Central Alps. *Chemical Geology*, 417, 322-340.
985 <https://doi.org/10.1016/j.chemgeo.2015.10.024>
- 986 Santosh, M., Tsunogae, T., Li, J.H., & Liu, S.J. (2007). Discovery of sapphirine-bearing Mg-
987 Al granulites in the North China Craton: implications for Paleoproterozoic ultrahigh
988 temperature metamorphism. *Gondwana Research*, 11, 263-285.
989 <https://doi.org/10.1016/j.gr.2006.10.009>
- 990 Santosh, M., & Omori, S. (2008). CO₂ flushing: a plate tectonic perspective. *Gondwana*
991 *Research*, 13, 86-102. <https://doi.org/10.1016/j.gr.2007.07.003>
- 992 Sawyer, E.W. (1994). Melt segregation in the continental crust. *Geology*, 22, 1019-1022.
993 [https://doi.org/10.1130/0091-7613\(1994\)022<1019:MSITCC>2.3.CO;2](https://doi.org/10.1130/0091-7613(1994)022<1019:MSITCC>2.3.CO;2)
- 994 Sawyer, E.W. (2008). *Atlas of migmatites*. The Canadian Mineralogist Special Publication 9.
995 Quebec: Mineralogical Association of Canada; Ottawa: NRC Research Press.
- 996 Sawyer, E.W., Cesare, B., & Brown M. (2011). When the continental crust melts. *Elements*,
997 7, 229-234. <https://doi.org/10.2113/gselements.7.4.229>
- 998 Scaillet, B., Holtz, F., Pichavant, M., & Schmidt, M. (1996). Viscosity of Himalayan
999 leucogranites: Implications for mechanisms of granitic magma ascent. *Journal of*
1000 *Geophysical Research: Solid Earth*, 101, 27691-27699.
1001 <https://doi.org/10.1029/96JB01631>
- 1002 Schmutz, H. (1976). Der Mafitit-Ultramafitit-Komplex zwischen Chiavenna und Val
1003 Bondasca (Provinz Sondrio, Italien; Kanton Graubünden, Schweiz). *Beiträge zur*
1004 *Geologischen Karte der Schweiz (N.F.)*, 149, 1-73. [https://doi.org/10.3929/ethz-a-](https://doi.org/10.3929/ethz-a-000085784)
1005 000085784
- 1006 Stevens, G., Clemens, J.D., & Droop, G.T.R. (1997). Melt production during granulite-facies
1007 anatexis: experimental data from “primitive” metasedimentary protoliths.

- 1008 *Contributions to Mineralogy and Petrology*, 128, 352-370.
- 1009 <https://doi.org/10.1007/s004100050314>
- 1010 Stevens, G., Villaros, A., & Moyen, J-F. (2007). Selective peritectic garnet entrainment as the
1011 origin of geochemical diversity in S-type granites. *Geology*, 35, 9-12.
- 1012 <https://doi.org/10.1130/G22959A.1>
- 1013 Tacchetto, T., Bartoli, O., Cesare, B., Berkesi, M., Aradi, L. E., Dumond, G., & Szabó, C.
1014 (2019). Multiphase inclusions in peritectic garnet from granulites of the Athabasca
1015 granulite terrane (Canada): Evidence of carbon recycling during Neoproterozoic crustal
1016 melting. *Chemical Geology*, 508, 197-209.
- 1017 <https://doi.org/10.1016/j.chemgeo.2018.05.043>
- 1018 Tajčmanová, L., Connolly, J. A. D., & Cesare, B. (2009). A thermodynamic model for
1019 titanium and ferric iron solution in biotite. *Journal of Metamorphic Geology*, 27, 153-
1020 165. <https://doi.org/10.1111/j.1525-1314.2009.00812.x>
- 1021 Tamic, N., Behrens, H., & Holtz, F. (2001). The solubility of H₂O and CO₂ in rhyolitic melts
1022 in equilibrium with a mixed CO₂-H₂O fluid phase. *Chemical geology*, 174, 333-347.
- 1023 [https://doi.org/10.1016/S0009-2541\(00\)00324-7](https://doi.org/10.1016/S0009-2541(00)00324-7)
- 1024 Taylor, S.R., & McLennan, S.M. (1995). The geochemical evolution of the continental crust.
1025 *Reviews of Geophysics*, 33, 241-265. <https://doi.org/10.1029/95RG00262>
- 1026 Teyssier, C., & Whitney, D. L. (2002). Gneiss domes and orogeny. *Geology*, 30, 1139-1142.
1027 [https://doi.org/10.1130/0091-7613\(2002\)030<1139:GDAO>2.0.CO;2](https://doi.org/10.1130/0091-7613(2002)030<1139:GDAO>2.0.CO;2)
- 1028 Thomen, A., Robert, F., & Remusat, L. (2014). Determination of the nitrogen abundance in
1029 organic materials by NanoSIMS quantitative imaging. *Journal of Analytical Atomic*
1030 *Spectrometry*, 29, 512-519. DOI: 10.1039/C3JA50313E
- 1031 Todd, C.S., & Engi, M. (1997). Metamorphic field gradients in the Central Alps. *Journal of*
1032 *metamorphic geology*, 15, 513-530. <https://doi.org/10.1111/j.1525-1314.1997.00038.x>

- 1033 Touret, J. L., & Huizenga, J. M. (2011). Fluids in granulites. *Geological Society of America*
1034 *Memoirs*, 207, 25-37. [https://doi.org/10.1130/2011.1207\(03\)](https://doi.org/10.1130/2011.1207(03))
- 1035 Trommsdorff, V., & Nievergelt, P. (1983). The Bregaglia (Bergell) Iorio intrusive and its
1036 field relations. *Memorie della Società Geologica Italiana*, 26, 55-68.
- 1037 Tulloch, A. J., Ramezani, J., Kimbrough, D. L., Faure, K., & Allibone, A. H. (2009). U-Pb
1038 geochronology of mid-Paleozoic plutonism in western New Zealand: Implications for
1039 S-type granite generation and growth of the east Gondwana margin. *Geological*
1040 *Society of America Bulletin*, 121, 1236-1261. <https://doi.org/10.1130/B26272.1>
- 1041 Turcotte, D., & Schubert, G. (2014). Geodynamics. Cambridge university press.
- 1042 Vielzeuf, D., & Holloway, J.R. (1988). Experimental determination of the fluid-absent
1043 melting relations in the pelitic system. *Contributions to Mineralogy and Petrology*,
1044 98, 257-276. <https://doi.org/10.1007/BF00375178>
- 1045 Vigneresse, J. L., Barbey, P., & Cuney, M. (1996). Rheological transitions during partial
1046 melting and crystallization with application to felsic magma segregation and transfer.
1047 *Journal of Petrology*, 37, 1579-1600. DOI: 10.1093/petrology/37.6.1579
- 1048 Visonà, D., & Lombardo, B. (2002). Two-mica and tourmaline leucogranites from the
1049 Everest–Makalu region (Nepal–Tibet). Himalayan leucogranite genesis by isobaric
1050 heating? *Lithos*, 62, 125-150. [https://doi.org/10.1016/S0024-4937\(02\)00112-3](https://doi.org/10.1016/S0024-4937(02)00112-3)
- 1051 Von Blanckenburg, F. (1992). Combined high-precision chronometry and geochemical
1052 tracing using accessory minerals: Applied to the Central-Alpine Bergell intrusion
1053 (Central Europe). *Chemical Geology*, 100, 19-40. [https://doi.org/10.1016/0009-](https://doi.org/10.1016/0009-2541(92)90100-J)
1054 [2541\(92\)90100-J](https://doi.org/10.1016/0009-2541(92)90100-J)
- 1055 Von Blanckenburg, F., Früh-Green, G., Diethelm, K., & Stille, P. (1992). Nd-, Sr-, O-

- 1056 isotopic and chemical evidence for a two-stage contamination history of mantle
1057 magma in the Central-Alpine Bergell intrusion. *Contributions to Mineralogy and*
1058 *Petrology*, 110, 33-45. <https://doi.org/10.1007/BF00310880>
- 1059 Wang, X., Ming Chou, I., Hu, W., Burruss, R.C., Sun, Q., & Song Y. (2011). Raman
1060 spectroscopic measurements of CO₂ density: experimental calibration with high-
1061 pressure optical cell (HPOC) and fused silica capillary capsule (FSCC) with
1062 application to fluid inclusion observations. *Geochimica et Cosmochimica Acta*, 75,
1063 4080-4093. <https://doi.org/10.1016/j.gca.2011.04.028>
- 1064 Wenk, E., (1955). Eine Strukturkarte der Tessiner Alpen. *Schweizerische und Mineralogische*
1065 *und Petrographische Mitteilungen*, 35, 311-319. [http://dx.doi.org/10.5169/seals-](http://dx.doi.org/10.5169/seals-27854)
1066 27854
- 1067 Whalen, J. B., Currie, K. L., & Chappell, B. W. (1987). A-type granites: geochemical
1068 characteristics, discrimination and petrogenesis. *Contributions to Mineralogy and*
1069 *Petrology*, 95, 407-419. <https://doi.org/10.1007/BF00402202>
- 1070 White, R.W., & Powell, R. (2002). Melt loss and the preservation of granulite facies material
1071 assemblages. *Journal of metamorphic geology*, 20, 621-632.
1072 https://doi.org/10.1046/j.1525-1314.2002.00206_20_7.x
- 1073 White, R.W., Stevens, G., & Johnson, T.E. (2011). Is the crucible reproducible? Reconciling
1074 melting experiments with thermodynamic calculations. *Elements*, 7, 241-246.
1075 <https://doi.org/10.2113/gselements.7.4.241>
- 1076 Yu, B., Santosh, M., Li, S. S., & Shaji, E. (2019). Petrology, phase equilibria modelling, and
1077 in situ zircon and monazite geochronology of ultrahigh-temperature granulites from
1078 the khondalite belt of southern India. *Lithos*, 348-349, 105195.
1079 <https://doi.org/10.1016/j.lithos.2019.105195>

1080 Zhang, H. F., Parrish, R., Zhang, L., Xu, W. C., Yuan, H. L., Gao, S., & Crowley, Q. G.
1081 (2007). A-type granite and adakitic magmatism association in Songpan–Garze fold
1082 belt, eastern Tibetan Plateau: implication for lithospheric delamination. *Lithos*, *97*,
1083 323-335. <https://doi.org/10.1016/j.lithos.2007.01.002>

1084

1085

1086 SUPPORTING INFORMATION

1087 Additional supporting information may be found online in the Supporting Information
1088 section.

1089 **Figure S1.** Garnet zoning in Type A and Type C granulites.

1090 **Figure S2.** Harker diagrams showing the complete set of MI analyses.

1091 **Figure S3.** CIPW Qz-Ab-Or diagram showing normative compositions for the analysed MI
1092 and reference analyses from the literature.

1093 **Figure S4.** Viscosities of rhyolitic melts vs. H₂O content.

1094 **Table S1.** Calculated densities of CO₂ within melt and fluid inclusions.

1095 **Table S2.** Major elements profiles for garnets of Type A and Type C granulites.

1096 **Table S3.** Chemical compositions of minerals in nanogranitoid inclusions.

1097 **Table S4.** Composition of peritectic and daughter minerals from experimental runs at
1098 different P-T-t conditions.

1099 **Table S5.** Chemical composition of re-homogenized and glassy melt inclusions.

1100 **Table S6.** Model parameters and calculated melt velocities

1101

1102

1103

1104

1105 **CAPTIONS FIGURES TEXT**

1106

1107 **FIGURE 1** Tectonic map of the Central Alps modified after Trommsdorff and Nievergelt
1108 (1983). Coordinates are given according to the Swiss geographical grid (units in kilometres).

1109

1110 **FIGURE 2** UHT granulites from the Gruf Complex. (a) Massive sapphirine-orthopyroxene-
1111 cordierite-garnet granulite (Type A) and (b) massive orthopyroxene-cordierite-garnet
1112 granulite (Type C).

1113

1114 **FIGURE 3** Photomicrographs of the granulites from the Gruf Complex. (a) Garnet
1115 porphyroblast from a Type A granulite showing a cluster of MI near to the core of the crystal
1116 (red box). (b) Zoom of the same cluster of MI as in (a). (c) Garnet porphyroblasts from a
1117 Type C granulite. The red box at the rim of the garnet indicate a cluster of MI. (d) Zoom of
1118 the same cluster of MI as in (c). (d) Plane-polarized light photomicrograph of MI in garnet.
1119 (e) Same as (d) under crossed-polarized light, showing multiple birefringent phases within
1120 the inclusions. (g) Fluid inclusions (FI) and MI within a cluster. (h) Glassy MI containing a
1121 CO₂ shrinkage bubble. (i) MI in a sapphirine porphyroblast from a Type A granulite.

1122

1123 **FIGURE 4** Raman spectra of nanogranitoids and glassy MI. (a) Glassy MI with a shrinkage
1124 bubble containing CO₂. (b) Analysis of a nanogranitoid inclusion (red circle) close to a glassy
1125 MI showing a shrinkage bubble. (c) Nanogranitoid with a CO₂ bubble. (d) Nanogranitoid in
1126 sapphirine. (e) Mixed inclusion (fluid + melt) showing CO together with phyllosilicates,
1127 quartz and Fe-magnesite. (f) Mixed inclusion with phyllosilicates, Fe-magnesite, CO₂ and N₂.

1128

1129 **FIGURE 5** Backscattered images of nanogranitoids. Nanogranitoids from Type A (a-d) and
1130 from Type C (e-f) granulites are shown.

1131

1132 **FIGURE 6** Backscattered images of experimentally remelted nanogranitoids. (a,b) Remelted
1133 MI with a well-developed negative shape. (c) Re-homogenized MI showing a trapped rutile
1134 needle, indenting the wall of the inclusion. (d) MI showing an irregular border and bubbles
1135 within the glass. (e,f) Partially remelted nanogranitoids, displaying daughter phases (biotite
1136 and quartz) and evidence of minor overheating (recrystallization of garnet and peritectic
1137 orthopyroxene). (g) Interaction of matrix melt with a garnet chip, forming peritectic
1138 orthopyroxene needles. (h) Melt pocket of infiltrated matrix melt within the garnet chip. The
1139 glass displays abundant bubbles. (i) MI from an experiment at 950°C showing strong
1140 evidence of overheating (formation of peritectic orthopyroxene and recrystallization of new
1141 garnet at the wall of the inclusion).

1142

1143 **FIGURE 7** Chemical classification of remelted and glassy MI from the Gruf Complex
1144 (normalized to 100% on anhydrous basis). Reported are MI analyses of re-melting
1145 experiments between 800 and 900°C with graphite-bearing (Gr) and quartz-bearing (Qz)
1146 capsules. (a) Aluminum saturation index vs. alkalinity index. (b) TAS diagram. Analyses for
1147 charnockites and leucogranites from the Gruf Complex are from Galli et al. (2013), whereas
1148 MI analyses from the Kerala Khondalite Belt are from Cesare et al. (2009) and Ferrero et al.
1149 (2012). Data for S-type granites (Chappel & White, 1992; Jung, Hoernes, & Mezger, 2000;
1150 Kalsbeek, Jepsen, & Jones, 2001; Tulloch, Ramezani, Kimbrough, Faure, & Allibone, 2009;
1151 Visonà & Lombardo, 2002) and for A-type granites (Castro et al., 2012; de Almeida, de
1152 Pinho Guimarães, & da Silva Filho, 2002; Florisbal, de Fátima Bitencourt, Nardi, &
1153 Conceição, 2009; Ghani et al., 2014; Goodenough, Upton, & Ellam, 2000; King, White,

1154 Chappell, & Allen, 1997; King, Chappell, Allen, & White, 2001; McDermott, Harris, &
1155 Hawkesworth, 2000; Whalen, Currie, & Chappell, 1987; Zhang et al., 2007) are also reported
1156 for comparison.

1157

1158 **FIGURE 8** Chemical composition of glasses from experimentally remelted and natural
1159 glassy inclusions (normalized to 100% on anhydrous basis). Reference analyses are the same
1160 as in Figure 7.

1161

1162 **FIGURE 9** H₂O and CO₂ content measured in remelted nanogranitoid inclusions. Error bars
1163 are displayed only when bigger than the symbol. Data for MI from the Ivrea Zone (Carvalho
1164 et al., 2019) are also reported for comparison (black dots = upper amphibolite facies, grey
1165 squares = transition zone, brown crosses = granulite facies).

1166

1167 **FIGURE 10** AKF diagram (after Vielzeuf & Holloway, 1988) projected from quartz for MI
1168 and bulk rocks. (a) Type A granulite. (b) Type C granulite. Also reported for comparison are:
1169 melt inclusions from the Kerala Khondalite Belt (Cesare et al., 2009; Ferrero et al., 2012),
1170 experimental glasses (900°C, 5 kbar) of Droop et al. (2003) and experimental glasses (875-
1171 1075°C, 7-13 kbar) of Patiño-Douce & Johnston (1991).

1172

1173

1174

1175

1176

1177

1178

1179 **CAPTIONS FIGURES SUPPORTING INFORMATION**

1180

1181 **Figure S1.** Compositional profiles of garnets in Type A and Type C granulites.

1182 **Figure S2.** Harker diagrams showing the complete set of MI analyses. Small symbols

1183 represent disregarded analyses. The line displayed for Al₂O₃, FeO and and MgO represents

1184 the tie-line between the host garnet (Type A granulite) and the average composition of the

1185 glassy inclusions (black triangle).

1186 **Figure S3.** CIPW Qz-Ab-Or diagram showing normative compositions for the analysed MI

1187 and other reference analyses from the literature (see text).

1188 **Figure S4.** Viscosities of rhyolitic melts vs. H₂O content (modified after Ardia et al., 2008).

1189 Viscosities for MI are calculated according to Giordano et al. (2008).

1190

1191

1192

1193

1 **Title: Anatectic melt inclusions in ultra-high temperature granulites**

2 **Omar Gianola**¹, Omar Bartoli¹, Fabio Ferri¹, Andrea Galli², Silvio Ferrero³, Luca S.

3 Capizzi^{1,4}, Christian Liebske², Laurent Remusat⁵, Stefano Poli⁶, Bernardo Cesare¹

4 ¹ Dipartimento di Geoscienze, Università degli Studi di Padova, Via G. Gradenigo 6, 35131 Padova,

5 Italy

6 ² Institute of Geochemistry and Petrology, ETH Zürich, Switzerland

7 ³ Institut für Erd- und Umweltwissenschaften, Universität Potsdam, Potsdam, Germany

8 ⁴ Dipartimento di Scienze della Terra, Università degli Studi di Roma “La Sapienza”, Roma, Italy

9 ⁵ Institut de Minéralogie, de Physique des Matériaux, et de Cosmochimie (IMPMC), UMR CNRS

10 7590 – Sorbonne Université – Muséum National d'Histoire Naturelle, Paris, France

11 ⁶ Dipartimento di Scienze della Terra “Ardito Desio”, Università degli Studi di Milano, Milano, Italy

12

13

14

15

16

17

18

19

20

21

	Type A granulites		Type C granulites	
	BRE-core	BRE-rim (glassy)	GRAG-core	GRAG-rim
No. analyses by EPMA / NanoSIMS	6 / 6	11	21 / 3	6 / 7
Wt%				
SiO ₂	70.08 (2.51)	75.33 (1.26)	74.90 (1.00)	71.93 (1.54)
TiO ₂	0.05 (0.04)	0.00 (0.01)	0.05 (0.04)	0.06 (0.07)
Al ₂ O ₃	14.45 (0.88)	12.87 (0.64)	11.75 (0.43)	13.29 (1.19)
FeO	1.67 (0.32)	0.91 (0.05)	1.52 (0.14)	1.93 (0.36)
MnO	0.05 (0.02)	0.05 (0.02)	0.02 (0.02)	0.08 (0.04)
MgO	0.54 (0.24)	0.10 (0.08)	0.71 (0.10)	0.53 (0.23)
CaO	0.94 (0.55)	0.05 (0.02)	0.51 (0.15)	0.55 (0.19)
Na ₂ O	1.96 (0.54)	1.66 (0.38)	0.73 (0.27)	0.72 (0.39)
K ₂ O	7.31 (1.43)	8.67 (0.82)	6.96 (0.48)	7.95 (1.88)
P ₂ O ₅	0.20 (0.18)	0.04 (0.03)	0.12 (0.06)	0.17 (0.15)
Cl	0.04 (0.03)	0.01 (0.00)	0.06 (0.02)	0.12 (0.04)
Total	97.31 (2.33)	99.70 (0.31)	97.33 (0.79)	97.33 (1.57)
H ₂ O by NanoSIMS [wt%]	6.20 (1.25)	-	7.05 (3.00)	4.35 (0.92)
CO ₂ by NanoSIMS [ppm]	779 (326)	-	1113 (843)	940 (407)
ASI	1.14 (0.13)	1.06 (0.03)	1.24 (0.07)	1.27 (0.19)
K#	71 (8)	77 (5)	87 (4)	87 (7)
Mg#	35 (8)	13 (8)	44 (4)	32 (11)
CIPW norm				
Quartz	27.04	31.56	40.98	34.15
Corundum	2.10	0.76	2.39	2.89
Orthoclase	43.23	51.23	41.13	46.98
Albite	16.59	14.02	6.16	6.13
Anorthite	3.31	0.00	1.73	1.65
Hypersthene	4.43	2.01	4.51	4.91
Ilmenite	0.10	0.01	0.09	0.11
Apatite	0.47	0.10	0.29	0.39

1

2 **TABLE 1** Average compositions of remelted and preserved glassy MI. Numbers in
3 parentheses refer to the standard error of the mean expressed as 2 σ . ASI = molar
4 $[\text{Al}_2\text{O}_3/(\text{CaO}+\text{Na}_2\text{O}+\text{K}_2\text{O})]$, K# = molar $[\text{K}_2\text{O}/(\text{K}_2\text{O}+\text{Na}_2\text{O})] \times 100$; Mg# = molar
5 $[\text{MgO}/(\text{MgO}+\text{FeO})] \times 100$.

1

Analysis	Sample	Approx. size	Homogeneity	H ₂ O [wt%]	1 σ error	CO ₂ [ppm]	1 σ error
<i>Type A granulites</i>							
C_MI1_Gr1	BRE17-B13 core	<10 μ m	Glass	5.52	0.04	460	20
C_MI3_Gr3_1	BRE17-B13 core	\geq 20 μ m	Glass + bubble	8.27	0.27	1164	33
C_MI3_Gr3_2	BRE17-B13 core	\geq 20 μ m	Glass + bubble	7.34	0.23	1064	31
C_MI16_Gr4	BRE17-B13 core	\geq 20 μ m	Glass + 10% crystals + bubble	6.88	0.21	1194	34
E_MI6_Gr2_1	BRE17-D2 core	<10 μ m	Glass	4.41	0.04	408	17
E_MI6_Gr2_2	BRE17-D2 core	<10 μ m	Glass	4.76	0.04	387	17
OG16_MI2_Gr1	BRE17-B13 rim	<10 μ m	Glass + 3% crystals	4.68	0.04	1153	32
<i>Type C granulites</i>							
A_MI1_Gr1	GRAG-P3 core	<10 μ m	Glass	8.75	0.07	1738	41
A_MI3_Gr2	GRAG-P3 core	<10 μ m	Glass + bubble	8.34	0.06	1291	33
A_MI2_Gr2	GRAG-P3 core	<10 μ m	Glass + 3% crystals	4.06	0.04	310	17
F_MI12_Gr1	GRAG-P2 Gr1 rim	10-20 μ m	Glass + 3% crystals	4.51	0.04	160	15
F_MI1_Gr4	GRAG-P2 Gr1 rim	<10 μ m	Glass + 2% crystals	2.88	0.04	1569	34
OG18_MI1_Gr4	GRAG-P3 rim	<10 μ m	Glass	3.11	0.04	1149	28
OG18_MI3_Gr4	GRAG-P3 rim	<10 μ m	Glass + bubble	3.44	0.04	1064	32
OG18_MI6_Gr1	GRAG-P3 rim	<10 μ m	Glass + 1% crystals	5.18	0.04	221	15
OG18_MI4_Gr2_1	GRAG-P3 rim	10-20 μ m	Glass	5.94	0.04	1287	31
OG18_MI4_Gr2_2	GRAG-P3 rim	10-20 μ m	Glass	5.41	0.04	1132	27

2

3 **TABLE 2** H₂O and CO₂ contents of re-homogenized MI determined by NanoSIMS.

4

5

6

7

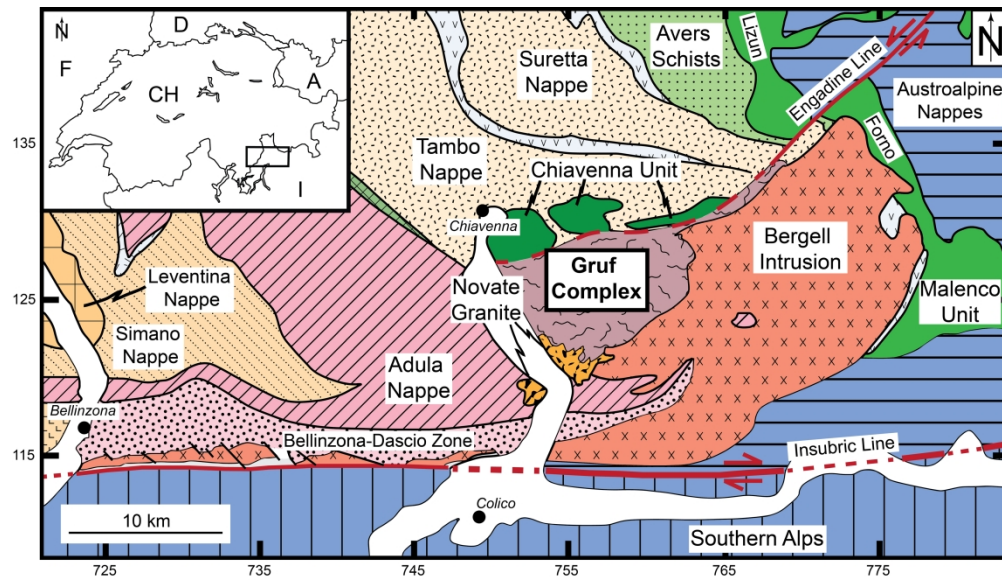


FIGURE 1 Tectonic map of the Central Alps modified after Trommsdorff and Nievergelt (1983). Coordinates are given according to the Swiss geographical grid (units in kilometres).

172x98mm (600 x 600 DPI)

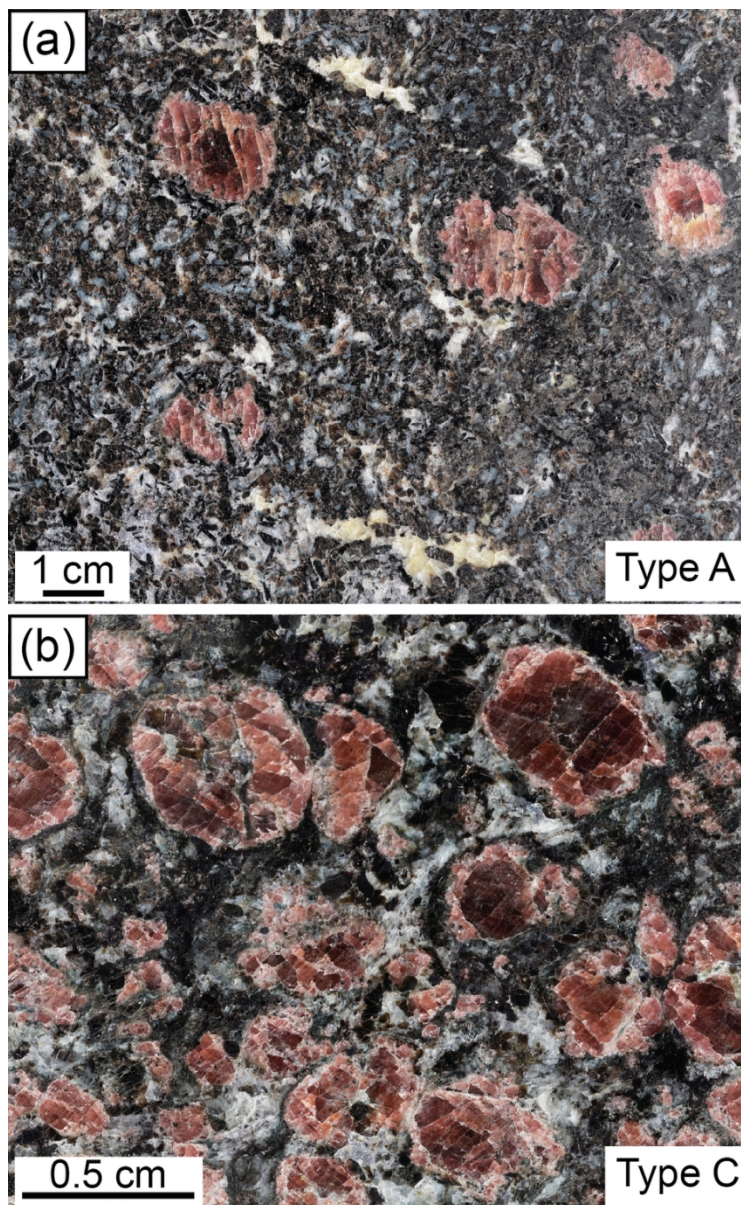


FIGURE 2 UHT granulites from the Gruf Complex. (a) Massive sapphirine-orthopyroxene-cordierite-garnet granulite (Type A) and (b) massive orthopyroxene-cordierite-garnet granulite (Type C).

80x129mm (300 x 300 DPI)

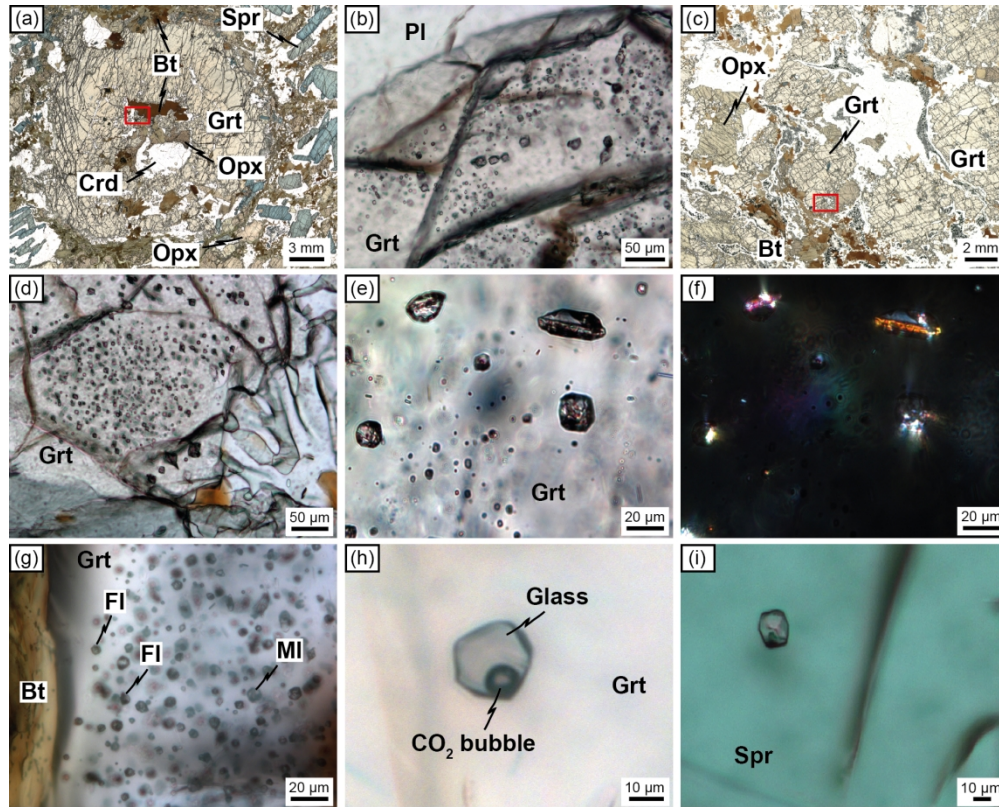


FIGURE 3 Photomicrographs of the granulites from the Gruf Complex. (a) Garnet porphyroblast from a Type A granulite showing a cluster of MI near to the core of the crystal (red box). (b) Zoom of the same cluster of MI as in (a). (c) Garnet porphyroblasts from a Type C granulite. The red box at the rim of the garnet indicate a cluster of MI. (d) Zoom of the same cluster of MI as in (c). (d) Plane-polarized light photomicrograph of MI in garnet. (e) Same as (d) under crossed-polarized light, showing multiple birefringent phases within the inclusions. (g) Fluid inclusions (FI) and MI within a cluster. (h) Glassy MI containing a CO₂ shrinkage bubble. (i) MI in a sapphirine porphyroblast from a Type A granulite.

166x133mm (300 x 300 DPI)

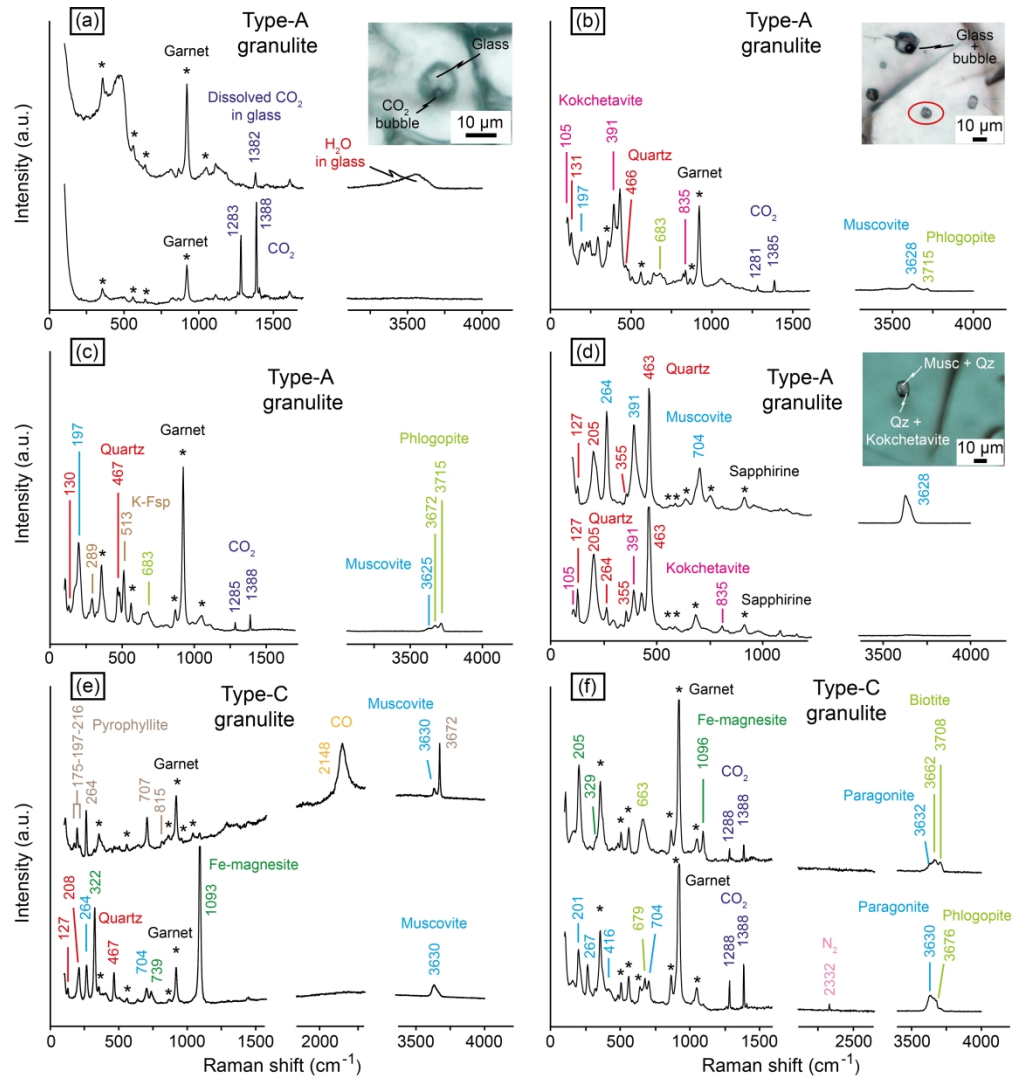


FIGURE 4 Raman spectra of nanogranitoids and glassy MI. (a) Glassy MI with a shrinkage bubble containing CO_2 . (b) Analysis of a nanogranitoid inclusion (red circle) close to a glassy MI showing a shrinkage bubble. (c) Nanogranitoid with a CO_2 bubble. (d) Nanogranitoid in sapphirine. (e) Mixed inclusion (fluid + melt) showing CO together with phyllosilicates, quartz and Fe-magnesite. (f) Mixed inclusion with phyllosilicates, Fe-magnesite, CO_2 and N_2 .

168x180mm (600 x 600 DPI)

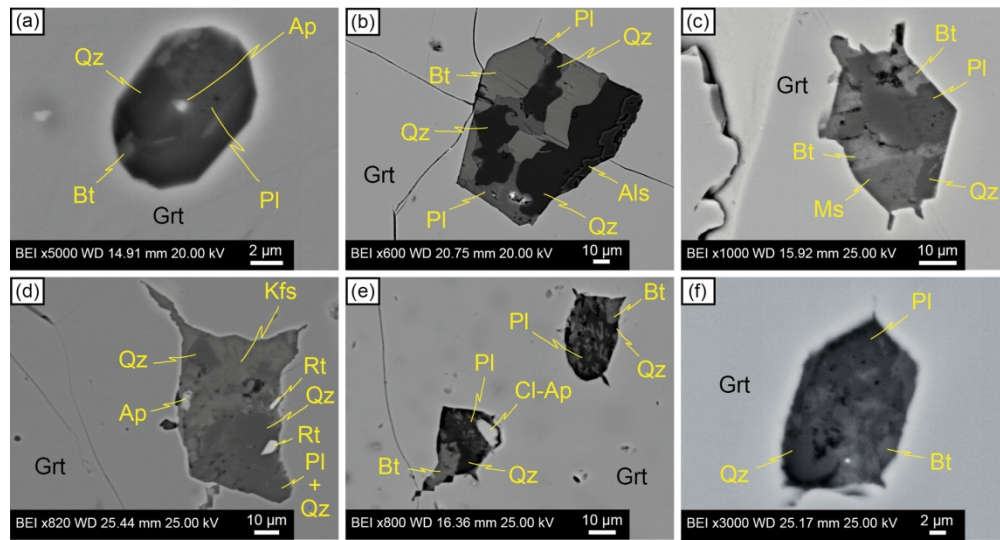


FIGURE 5 Backscattered images of nanogranitoids. Nanogranitoids from Type A (a-d) and from Type C (e-f) granulites are shown.

168x89mm (300 x 300 DPI)

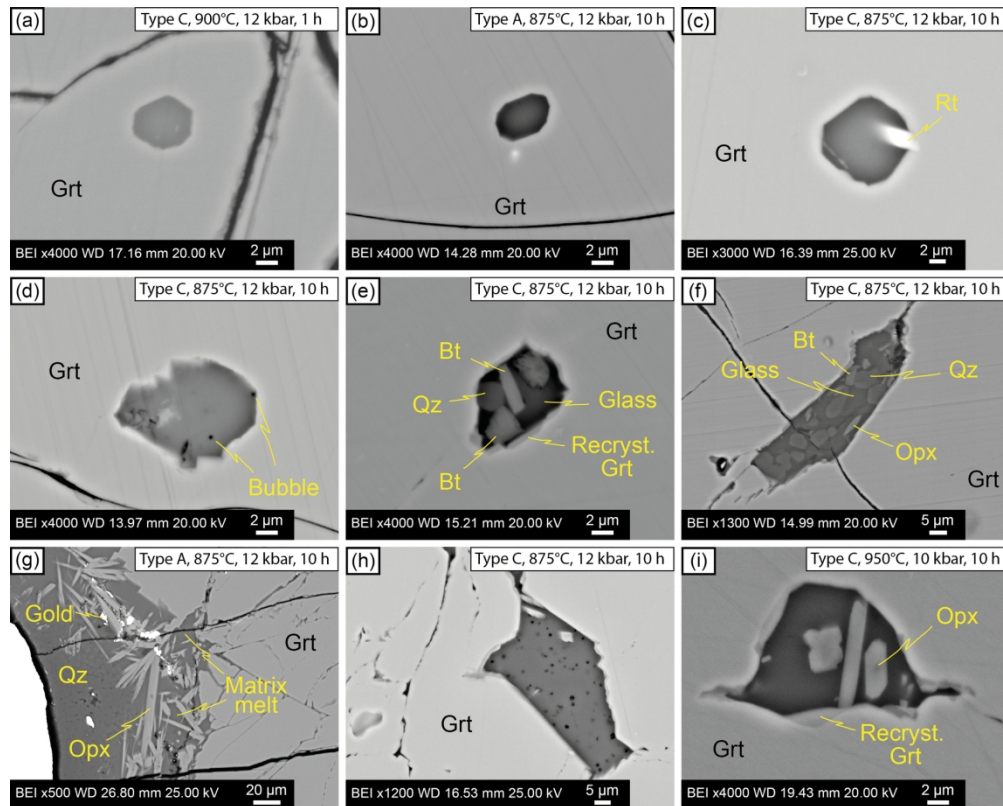


FIGURE 6 Backscattered images of experimentally remelted nanogranitoids. (a,b) Remelted MI with a well-developed negative shape. (c) Re-homogenized MI showing a trapped rutile needle, indenting the wall of the inclusion. (d) MI showing an irregular border and bubbles within the glass. (e,f) Partially remelted nanogranitoids, displaying daughter phases (biotite and quartz) and evidence of minor overheating (recrystallization of garnet and peritectic orthopyroxene). (g) Interaction of matrix melt with a garnet chip, forming peritectic orthopyroxene needles. (h) Melt pocket of infiltrated matrix melt within the garnet chip. The glass displays abundant bubbles. (i) MI from an experiment at 950°C showing strong evidence of overheating (formation of peritectic orthopyroxene and recrystallization of new garnet at the wall of the inclusion).

168x135mm (300 x 300 DPI)

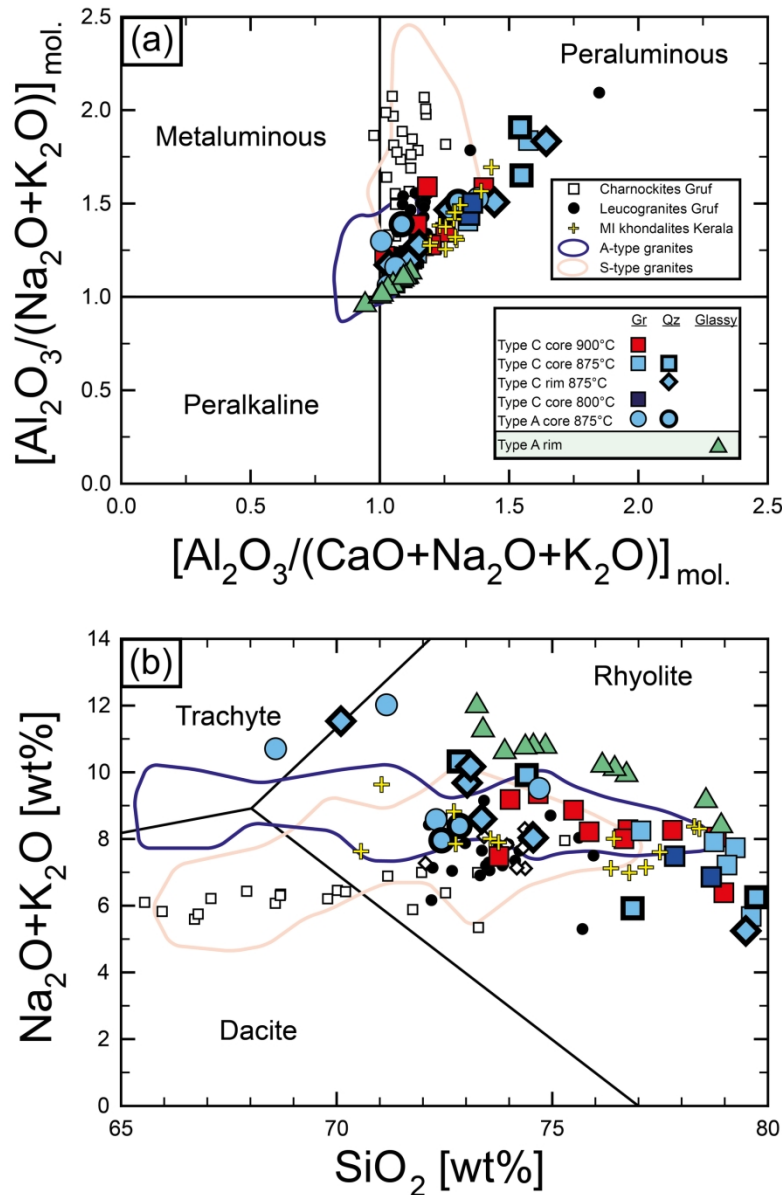


FIGURE 7 Chemical classification of remelted and glassy MI from the Gruf Complex (normalized to 100% on anhydrous basis). Reported are MI analyses of re-melting experiments between 800 and 900°C with graphite-bearing (Gr) and quartz-bearing (Qz) capsules. (a) Aluminum saturation index vs. alkalinity index. (b) TAS diagram. Analyses for charnockites and leucogranites from the Gruf Complex are from Galli et al. (2013), whereas MI analyses from the Kerala Khondalite Belt are from Cesare et al. (2009) and Ferrero et al. (2012). Data for S-type granites (Chappel & White, 1992; Jung, Hoernes, & Mezger, 2000; Kalsbeek, Jepsen, & Jones, 2001; Tulloch, Ramezani, Kimbrough, Faure, & Allibone, 2009; Visonà & Lombardo, 2002) and for A-type granites (Castro et al., 2012; de Almeida, de Pinho Guimarães, & da Silva Filho, 2002; Florisbal, de Fátima Bitencourt, Nardi, & Conceição, 2009; Ghani et al., 2014; Goodenough, Upton, & Ellam, 2000; King, White, Chappell, & Allen, 1997; King, Chappell, Allen, & White, 2001; McDermott, Harris, & Hawkesworth, 2000; Whalen, Currie, & Chappell, 1987; Zhang et al., 2007) are also reported for comparison.

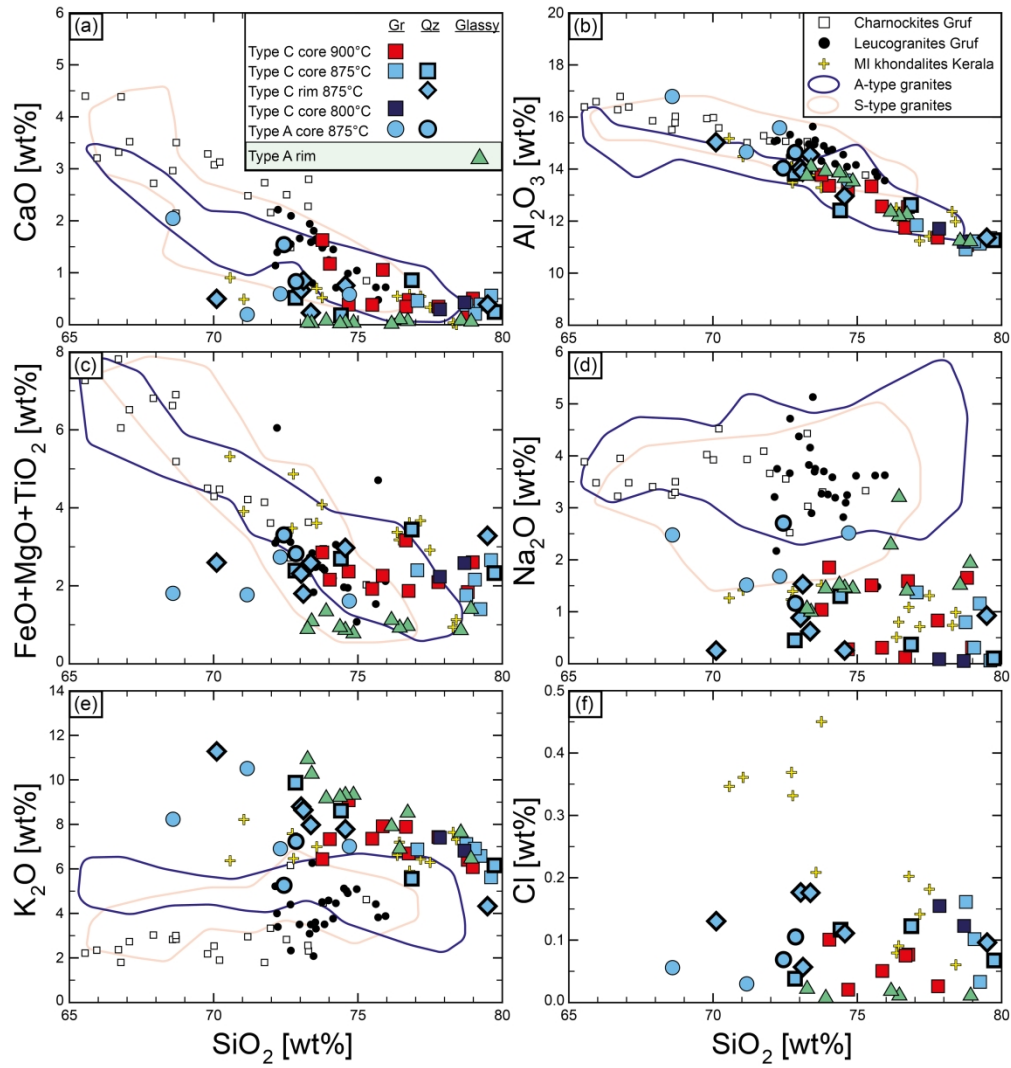


FIGURE 8 Chemical composition of glasses from experimentally remelted and natural glassy inclusions (normalized to 100% on anhydrous basis). Reference analyses are the same as in Figure 7.

169x180mm (600 x 600 DPI)

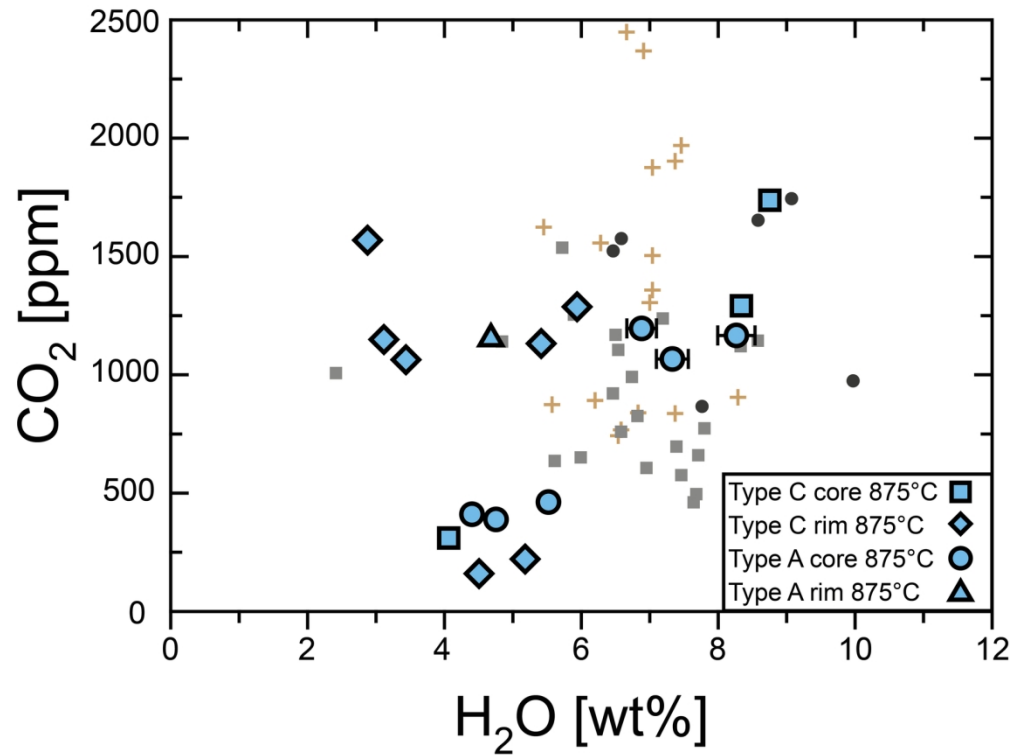


FIGURE 9 H₂O and CO₂ content measured in remelted nanogranitoid inclusions. Error bars are displayed only when bigger than the symbol. Data for MI from the Ivrea Zone (Carvalho et al., 2019) are also reported for comparison (black dots = upper amphibolite facies, grey squares = transition zone, brown crosses = granulite facies).

78x59mm (600 x 600 DPI)

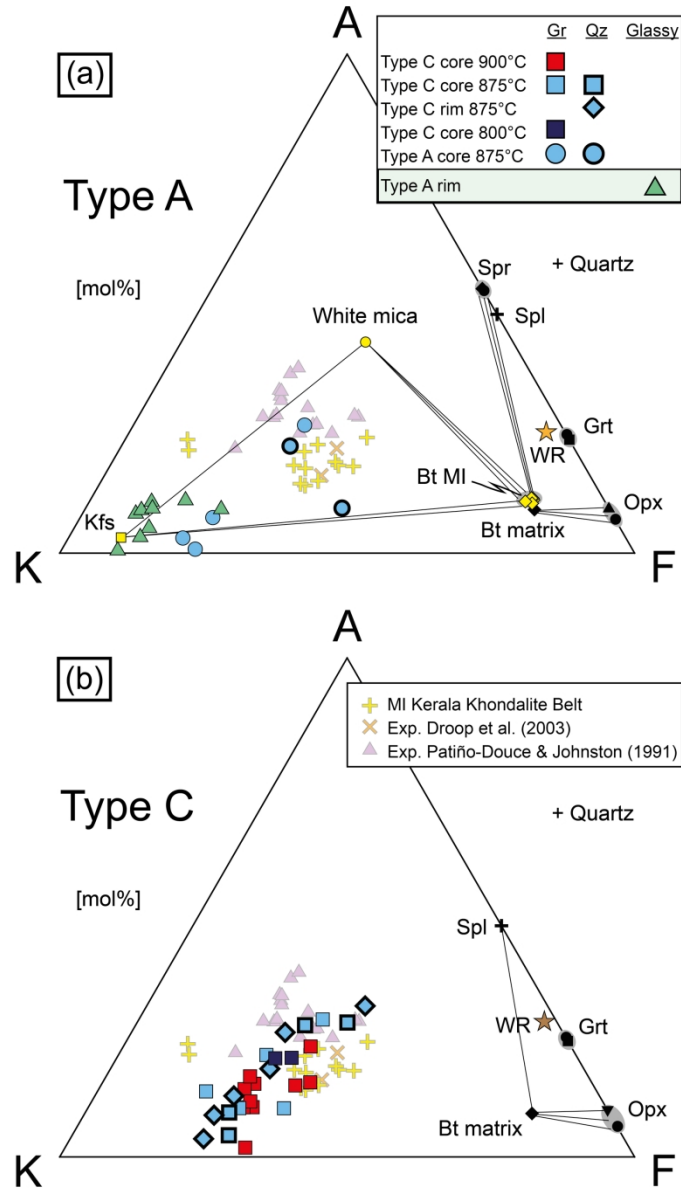
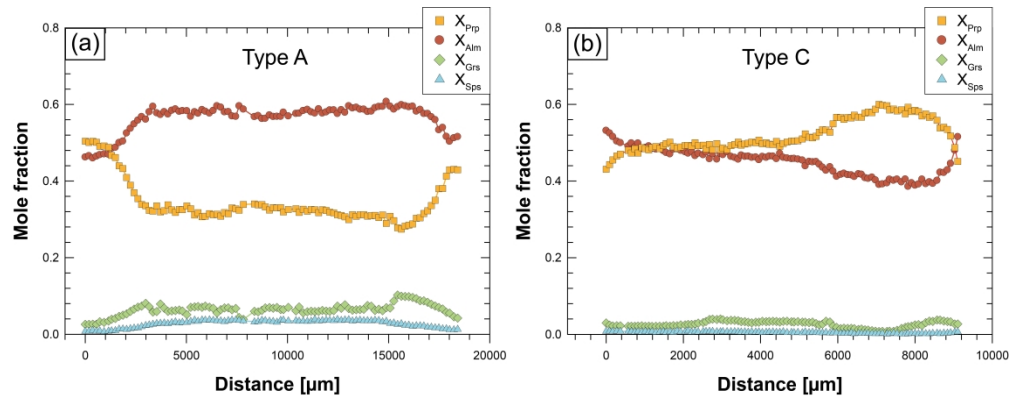
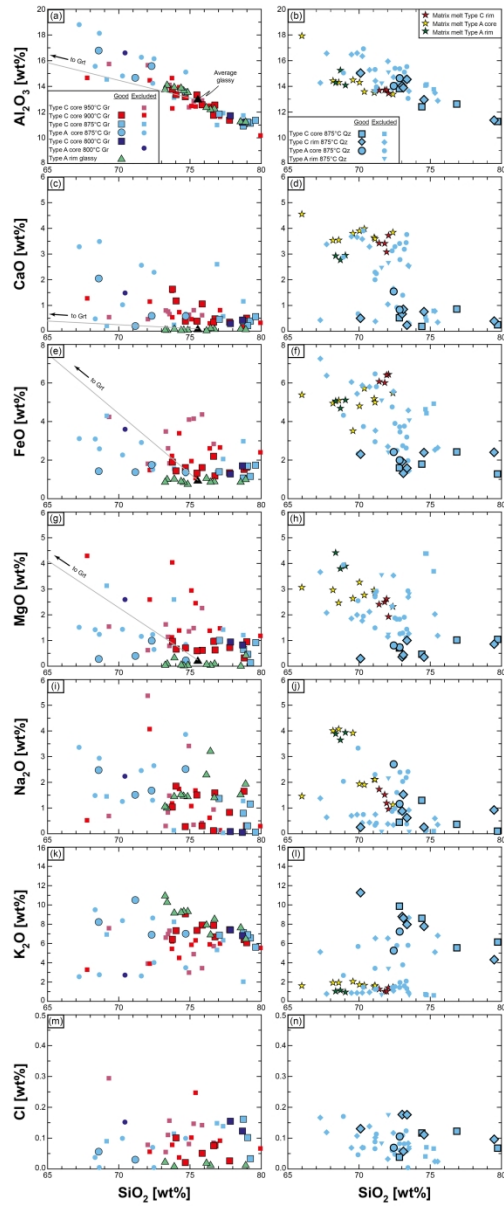


FIGURE 10 AKF diagram (after Vielzeuf & Holloway, 1988) projected from quartz for MI and bulk rocks. (a) Type A granulite. (b) Type C granulite. Also reported for comparison are: melt inclusions from the Kerala Khondalite Belt (Cesare et al., 2009; Ferrero et al., 2012), experimental glasses (900°C, 5 kbar) of Droop et al. (2003) and experimental glasses (875-1075°C, 7-13 kbar) of Patiño-Douce & Johnston (1991).

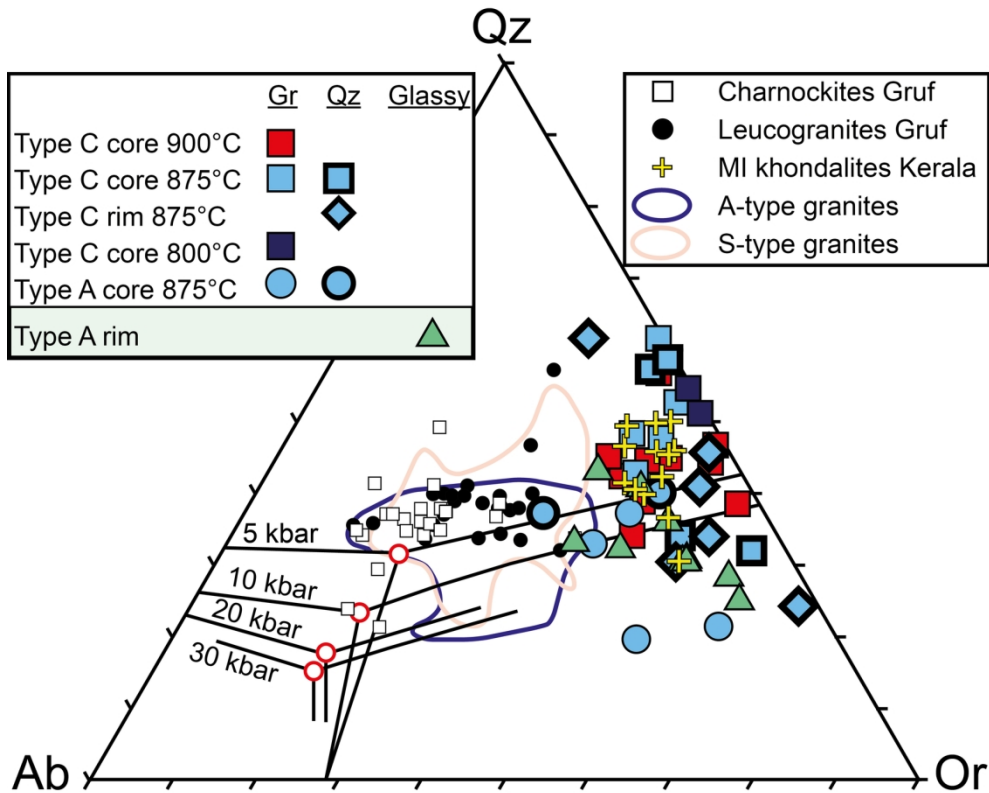
77x138mm (600 x 600 DPI)



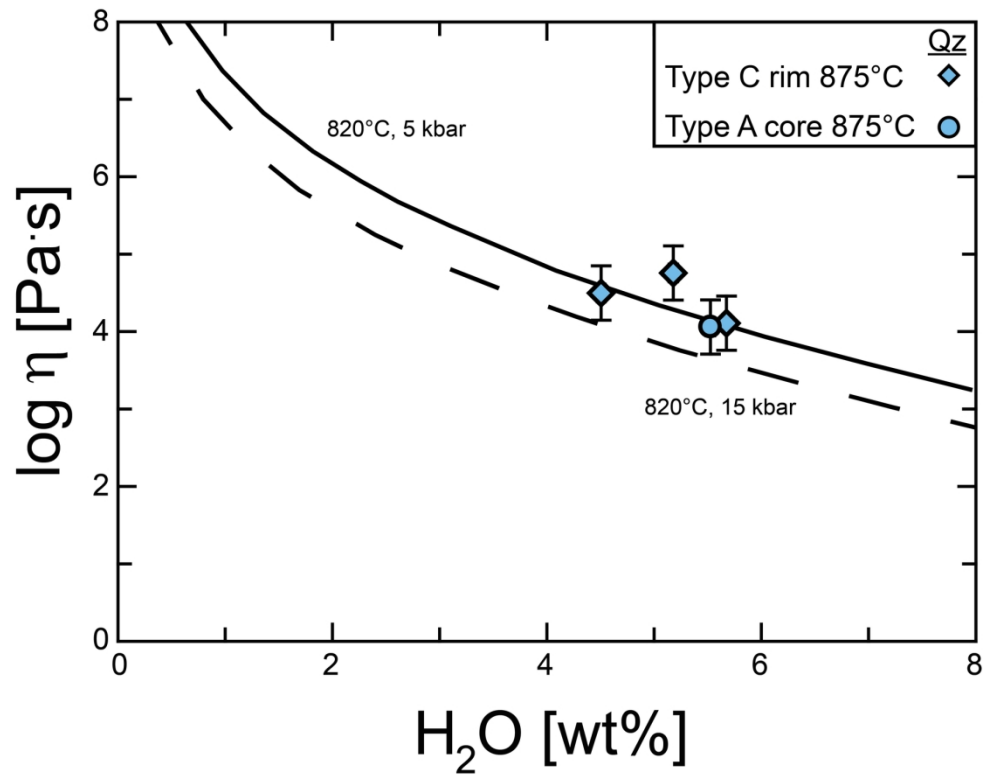
293x114mm (600 x 600 DPI)



169x411mm (300 x 300 DPI)



78x63mm (600 x 600 DPI)



81x63mm (600 x 600 DPI)